

1           Assessing the Sensitivity of Aerosol Mass Budget and  
2           Effective Radiative Forcing to Horizontal Grid Spacing in  
3           E3SMv1 Using A Regional Refinement Approach

4   Jianfeng Li<sup>1,\*</sup>, Kai Zhang<sup>1,\*</sup>, Taufiq Hassan<sup>1</sup>, Shixuan Zhang<sup>1</sup>, Po-Lun Ma<sup>1</sup>, Balwinder Singh<sup>1</sup>,  
5   Qiyang Yan<sup>1,a</sup>, Huilin Huang<sup>1</sup>

6   <sup>1</sup>Atmospheric Sciences and Global Change Division, Pacific Northwest National Laboratory,  
7   Richland, Washington, US

8   <sup>a</sup>now at KLA Corporation, US

9

10   \* Correspondence to Jianfeng Li (jianfeng.li@pnnl.gov) and Kai Zhang (Kai.Zhang@pnnl.gov)

11

## 12 **Abstract**

13 Atmospheric aerosols have important impacts on air quality and the Earth-atmospheric energy  
14 balance. However, as computing power is limited, Earth system models generally use coarse spatial grids  
15 and parameterize finer-scale atmospheric processes. These parameterizations and the simulation of  
16 atmospheric aerosols are often sensitive to model horizontal resolutions. Understanding the sensitivities is  
17 necessary for the development of Earth system models at higher resolutions with the deployment of more  
18 powerful supercomputers. Using the Energy Exascale Earth System Model (E3SM) version 1, this study  
19 investigates the impact of horizontal grid spacing on the simulated aerosol mass budget, aerosol-cloud  
20 interactions, and the effective radiative forcing of anthropogenic aerosols ( $ERF_{\text{aer}}$ ) over the contiguous  
21 United States. We examine the resolution sensitivity by comparing the nudged simulation results for 2016  
22 from the low-resolution model (LR) and the regional refinement model (RRM).

23 As expected, the simulated emissions of natural dust, sea salt, and marine organic matter are  
24 substantially higher in the RRM than in the LR. In addition, RRM simulates stronger aqueous-phase  
25 production of sulfate through the enhanced oxidation of sulfur dioxide by hydrogen peroxide due to  
26 increased cloud liquid water content. In contrast, the gas-phase chemical production of sulfate is slightly  
27 suppressed. The RRM resolves more large-scale precipitation and produces less convective precipitation  
28 than the LR, leading to increased (decreased) aerosol wet scavenging by large-scale (convective)  
29 precipitation.

30 Regarding aerosol effects on clouds, RRM produces larger temporal variabilities of large-scale liquid  
31 cloud fractions than LR, resulting in increased microphysical cloud processing of aerosols (more  
32 interstitial aerosols are converted to cloud-borne aerosols via aerosol activation) in RRM. Water vapor  
33 condensation is also enhanced in RRM compared to LR. Consequently, the RRM simulation produces  
34 more cloud droplets, a larger cloud droplet radius, a higher liquid water path, and a larger cloud optical  
35 depth than the LR simulation. A comparison of the present-day and pre-industrial simulations indicates

36 that, for this contiguous United States domain, the higher resolution increases  $ERF_{aer}$  at the top of the  
37 model by about 12%, which is mainly attributed to the strengthened indirect effect associated with  
38 aerosol-cloud interactions.

## 39 **1 Introduction**

40 Atmospheric aerosols have played essential roles in the deterioration of air quality in recent decades,  
41 especially in rapidly developing countries (Li et al., 2019; Lim et al., 2020; Xiao et al., 2021). Besides  
42 directly degrading atmospheric visibility and with substantial impacts on human health (Apte et al., 2015;  
43 Wang et al., 2019), aerosols are also involved in the formation of other major atmospheric pollutants,  
44 such as ozone and nitrogen oxides (Perring et al., 2013; Pusede et al., 2015). In addition, atmospheric  
45 aerosols from natural and anthropogenic sources considerably affect the radiation balance of the Earth  
46 system. The present-day (PD) (the year 2014) anthropogenic aerosol effective radiative forcing ( $ERF_{aer}$ )  
47 relative to the pre-industrial (PI) period (the year 1850) is estimated to range from  $-0.63$  to  $-1.37$   $W\ m^{-2}$   
48 according to 17 Earth system models (ESMs) participating the Coupled Model Intercomparison Project  
49 Phase 6 (CMIP6) (Smith et al., 2020). Aerosols can modulate the earth-atmospheric energy balance via  
50 several pathways. Firstly, they directly scatter and absorb shortwave and longwave radiation. Secondly,  
51 they are involved in cloud formation by acting as cloud condensation nuclei (CCN) and ice nuclei, thus  
52 influencing cloud radiative forcing. Thirdly, light-absorbing aerosols depositing on snow and ice surfaces  
53 can change the snow and ice melting by absorbing more solar radiation, leading to changes in surface  
54 albedo and energy budgets (Qian et al., 2015). Aerosols can also indirectly affect the global energy  
55 budget by influencing the ocean biogeochemistry and terrestrial ecosystems (Hamilton et al., 2022;  
56 Jickells et al., 2005; Mahowald et al., 2017).

57 Accurate simulation of atmospheric aerosols in ESMs is challenging due to complex physical and  
58 chemical processes (e.g., emissions, nucleation, coagulation, condensation, dry deposition, wet  
59 scavenging and resuspension, droplet activation, gas- and aqueous-phase chemistry, and radiation) and  
60 our incomplete understanding of these processes. Substantial parameterizations are designed to represent  
61 the aerosol lifecycle and its interactions with clouds and radiation in the Energy Exascale Earth System  
62 Model (E3SM) (Burrows et al., 2022; Wang et al., 2020) — a state-of-the-science ESM sponsored by the

63 United States (US) Department of Energy (DOE) for scientific and energy mission applications (Golaz et  
64 al., 2022; Golaz et al., 2019). However, these parameterizations are primarily developed and evaluated at  
65 ESM scales, and their performance at higher resolution is generally unclear. As the computing power  
66 continues to increase, future ESMs are expected to run at much higher resolutions (Caldwell et al., 2021;  
67 Dueben et al., 2020; Heinzeller et al., 2016). Therefore, it is crucial to understand the fidelity of these  
68 aerosol parameterizations and how the simulated aerosol lifecycle and aerosol effects on cloud and  
69 radiation will change as model resolution increases. These efforts are critical for parameter tuning and  
70 model development at high resolutions (Caldwell et al., 2019; Ma et al., 2014; Ma et al., 2015).

71 Caldwell et al. (2019) and Feng et al. (2022) investigated the impacts of model horizontal resolutions  
72 on some aspects of the aerosol lifecycle in E3SM. However, both studies were based on simulations with  
73 global uniform resolutions, which will be computationally expensive when the model resolution increases  
74 further to convection-permitting. To reduce the computational cost and maintain high-resolution features,  
75 variable-resolution techniques with high-resolution grids in the region of interest transitioning to low-  
76 resolution meshes in others have been widely applied in ESMs (Harris et al., 2016; Schwartz, 2019;  
77 Zarzycki et al., 2014). Tang et al. (2019) developed a regional refinement model (RRM) configuration for  
78 E3SM version 1 (E3SMv1) with high-resolution meshes (~25 km) over the contiguous US (CONUS) and  
79 low-resolution meshes (~100 km) in other areas. They found that RRM highly resembles the uniform  
80 high-resolution simulation in the refined region, indicating that RRM can be an effective and  
81 computationally efficient configuration for high-resolution model development.

82 This study investigates the impact of horizontal grid spacing on aerosol mass budget, aerosol-cloud  
83 interactions, and  $ERF_{aer}$  over the CONUS in 2016 using the RRM configuration. We compare E3SMv1  
84 simulations with a global uniform grid spacing of ~100 km (hereafter referred to as the low-resolution  
85 (LR) simulations) to the RRM simulations using the same configuration as Tang et al. (2019) with higher  
86 resolution (~25km) meshes over CONUS. Our findings provide insights into aerosol parameterization  
87 development and their dependence on model horizontal resolution. The paper is organized as follows.

88 Section 2 describes the E3SMv1 model and the simulation configurations. Section 3 discusses the impacts  
89 of increasing resolution on 1) the natural aerosol sources, 2) the aerosol wet scavenging, 3) the aerosol  
90 chemical production, 4) the aerosol-cloud interactions, and 5)  $ERF_{acr}$ , where apparent discrepancies are  
91 found between the LR and RRM simulations. Finally, the study is summarized in Section 4.

## 92 **2 Model setup**

### 93 **2.1 E3SMv1 model description**

94 Aerosol processes are primarily represented in the E3SM Atmosphere Model version 1 (EAMv1)  
95 (Rasch et al., 2019), which uses the High-Order Methods Modeling Environment (HOMME) Spectral  
96 Element dynamical core (Dennis et al., 2012). The dynamical core and the physics parametrizations are  
97 computed on cubed-sphere grids with data stored at Gauss-Lobatto-Legendre (GLL) nodes. The EAMv1  
98 standard low-resolution configuration has 30 spectral elements per cube face (ne30) and 4 GLL nodes per  
99 spectral element (np4), corresponding to a horizontal grid spacing of  $\sim 100$  km. The model has 72 vertical  
100 layers with a vertical resolution of  $\sim 20$  m near the surface and a vertical resolution higher than 200 m  
101 below 1.5 km, and the model top reaches up to  $\sim 60$  km ( $\approx 0.1$  hPa). The model uses an updated version of  
102 the Zhang and McFarlane (1995) (ZM) deep convection scheme with a modified dilute plume calculation  
103 (Neale et al., 2008), the Cloud Layers Unified By Binormals (CLUBB) scheme for turbulence, shallow  
104 convection, and stratiform clouds (Bogenschütz et al., 2013; Golaz et al., 2002; Larson et al., 2002; Xie et  
105 al., 2018), the version 2 of the Morrison and Gettelman (2008) (MG2) 2-moment cloud microphysics  
106 scheme with a classical-nucleation-theory-based ice nucleation parameterization (Hoose et al., 2010;  
107 Wang et al., 2014), the revised version of the four-mode version of the Modal Aerosol Module (MAM4)  
108 (Liu et al., 2016; Wang et al., 2020), and the Rapid Radiative Transfer Model for GCMs (RRTMG)  
109 (GCM: general circulation model) (Iacono et al., 2008; Mlawer et al., 1997).

110 MAM4 considers seven aerosol species: mineral dust, sea salt, marine organic matter (MOM), black  
111 carbon (BC), primary organic matter (POM), secondary organic aerosol (SOA), and sulfate (SO<sub>4</sub>) (Wang  
112 et al., 2020). Dust emission is parameterized as a function of surface wind speed, soil erodibility, friction  
113 velocity, and a friction velocity threshold following the scheme of Zender et al. (2003) in the land  
114 component of E3SMv1. The emissions of sea salt and MOM are estimated from sea spray fluxes, which  
115 are parameterized as a function of surface wind speed and sea surface temperature (Burrows et al., 2022).  
116 Emissions of other aerosol species and precursor gases are prescribed using CMIP6 emission datasets  
117 (Hoesly et al., 2018; Van Marle et al., 2017). The physical properties (including the size distribution,  
118 density, and hygroscopicity) of the seven aerosol species are summarized in Burrows et al. (2022).  
119 MAM4 represents aerosol particles in four modes with distinct size properties: Aitken mode,  
120 accumulation mode, coarse mode, and primary carbon mode (Burrows et al., 2022; Liu et al., 2016; Wang  
121 et al., 2020). The primary carbon mode is specified for freshly emitted BC, POM, and MOM, the aging of  
122 which is treated explicitly — a feature different from the three-mode version of MAM (MAM3) (Liu et  
123 al., 2012). The Aitken mode consists of sea salt, MOM, SOA, and SO<sub>4</sub>, while all seven species can exist  
124 in accumulation and coarse modes. MAM4 assumes that aerosol species are internally mixed within each  
125 mode but externally mixed across different modes. Aerosol particles in each mode can suspend in the air  
126 (i.e., interstitial aerosols) or exist in cloud droplets (i.e., cloud-borne aerosols). The evolution of aerosol  
127 particles involves many physical and chemical processes, such as emissions, nucleation, coagulation,  
128 condensation, convective transport, activation, dry deposition, wet scavenging, resuspension, and gas-  
129 phase and aqueous chemistry. More details of these processes and their interactions with radiation and  
130 cloud microphysics are described in Liu et al. (2012), Liu et al. (2016), Wang et al. (2020), and Zhang et  
131 al. (2022a).

132 EAMv1 has been evaluated against observations and other ESMs in Xie et al. (2018), Rasch et al.  
133 (2019), and Golaz et al. (2019). The simulation of aerosol properties and ERF<sub>aer</sub> have been evaluated in  
134 Table S1 and Figures S1-S2, Wang et al. (2020), Burrows et al. (2022), Feng et al. (2022), and Zhang et

135 al. (2022a). Our investigation focuses on comparing LR and RRM simulations, and the known model  
136 biases, such as the dry biases over the Great Plains of the US, the Amazon region, and Southeast Asia  
137 (Xie et al., 2018) and the cold bias between the 1950s and the 2000s (Golaz et al., 2019), are not expected  
138 to affect the overall model sensitivity to the resolution change.

## 139 **2.2 E3SMv1 LR and RRM simulations**

140 In addition to the standard LR E3SMv1 simulation with a globally uniform resolution of ~100 km  
141 for EAMv1 and the land component, we conduct an RRM simulation following the configuration of Tang  
142 et al. (2019) with a relatively high-resolution mesh (~25 km) over the CONUS for the atmospheric and  
143 land components (Figure 1). The simulation period is from October 1, 2015, to January 1, 2017, with the  
144 first three months as model spin-up (Zhang et al., 2022a). The component set used in the simulations  
145 comprises the coupling of an active atmospheric component — EAMv1, an active land component  
146 (version 4.5 of the Community Land Model — CLM4.5) (Oleson et al., 2013), a simplified active sea ice  
147 component, and a data ocean model with prescribed historical sea surface temperature and sea ice  
148 fractions (Hurrell et al., 2008).

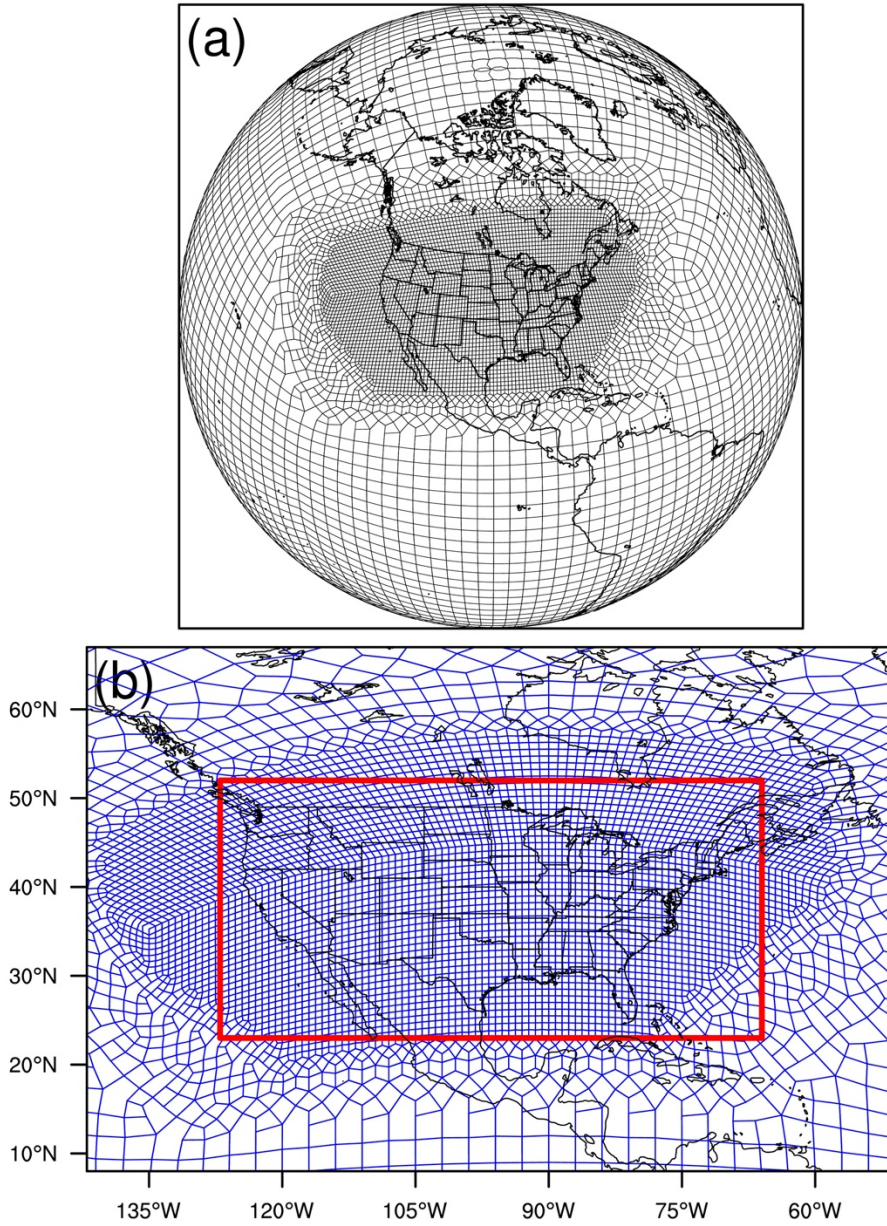
149 The atmospheric and land initial conditions in the LR simulation are derived from an earlier  
150 E3SMv1 simulation, which has reached equilibrium. The RRM initial conditions are regridded from those  
151 of the LR simulation to exclude the potential impact of distinct initial conditions on the simulation results.  
152 Anthropogenic and biomass-burning emissions of BC, POM, and SO<sub>4</sub> and precursor gas sulfur dioxide  
153 (SO<sub>2</sub>) are from the CMIP6 emission inventory (Feng et al., 2020; Hoesly et al., 2018). Notably, we use  
154 the emission data in 2014 instead of in 2016 due to the data availability of CMIP6. Dimethyl sulfide  
155 (DMS) emissions in 1850, 2000, and 2100 are estimated from a coupled model simulation with a detailed  
156 representation of DMS formation in the seawater (Wang et al., 2018). We obtain the DMS emissions in  
157 2014 through linear interpolation of the emissions in 1850, 2000, and 2100. The 3-D SOA production  
158 rates (implemented similarly to emissions) are derived from the simulation from Shrivastava et al. (2015).

159 Besides the PD LR and RRM simulations, we run two corresponding simulations with PI aerosol  
160 emissions to calculate  $ERF_{aer}$ . The PI simulation configurations are the same as the corresponding PD  
161 simulations except that emissions of BC, POM,  $SO_4$ ,  $SO_2$ , DMS, and SOA (production) in 1850 are used  
162 in the PI simulations.

163 We apply nudging globally in the LR and RRM simulations, which differs from Tang et al. (2019),  
164 which used nudging only on the low-resolution meshes but not the high-resolution grids in CONUS. We  
165 follow the nudging strategy from Zhang et al. (2014) and Sun et al. (2019), which demonstrated that a  
166 simulation with constraint horizontal winds could reproduce the evolution characteristics of the observed  
167 weather events and the model's long-term climatology. In addition, it has been corroborated that nudged  
168 simulations with a relatively short simulation period (e.g., one year) can reproduce the annual mean  
169 changes in aerosol burdens and optical depths caused by anthropogenic aerosols in the E3SM  
170 Atmospheric Model Intercomparison Project (AMIP) simulations (Zhang et al., 2022a). The short nudged  
171 simulations also have a similar estimate of  $ERF_{aer}$  as the AMIP-type free-running simulations (Zhang et  
172 al., 2022a). Moreover, by constraining the large-scale circulation, nudging helps suppress the noises  
173 caused by the chaotic response to model changes and facilitates the comparison between the LR and RRM  
174 simulations. Similarly, nudging is also used to estimate  $ERF_{aer}$ , as recommended by previous studies  
175 (Kooperman et al., 2012; Sun et al., 2019; Zhang et al., 2014). In short, nudging helps increase the signal-  
176 to-noise ratio and identify the impact caused by regional refinement more quickly. In our simulations, the  
177 horizontal winds are nudged toward the European Centre for Medium-Range Weather Forecasts  
178 Reanalysis v5 (ERA5) (Hersbach et al., 2020) with a relaxation time of 6 hours (Zhang et al., 2022b). To  
179 avoid the errors caused by vertical interpolation-extrapolation from ERA5 to E3SM vertical levels, we  
180 don't apply nudging for model levels below 950 hPa and above 10 hPa.

181 Several parameters differ between the E3SMv1 standard LR and CONUS RRM default  
182 configurations. For example, the time step for most physical processes and the coupling between physics  
183 and dynamics is 30 minutes in the LR configuration. In comparison, CONUS RRM uses a time step of 15

184 minutes. Many physical processes are sensitive to the time step and parameter setting (Wan et al., 2015;  
185 Wan et al., 2021; Zhao et al., 2013). Our sensitivity tests show substantial differences in the aerosol mass  
186 and energy budgets even outside of the refined region when the respective default configurations are used  
187 in the LR and RRM simulations, which is mainly attributed to their distinct physical time steps (not  
188 shown). Therefore, it would be better to keep the tuning parameters and time step the same between the  
189 LR and RRM simulations to isolate the regional refinement effect (horizontal resolution sensitivity), as  
190 recommended by earlier studies (Caldwell et al., 2021; Ma et al., 2015). Therefore, for the LR simulation,  
191 we use the time step of 15 minutes and the parameter setting from the default CONUS RRM  
192 configuration. With such changes, LR shares the same configuration as RRM, except for regional  
193 refinement around CONUS (Figure 1) and resolution-relevant input files (e.g., topography and nudging-  
194 prescribed wind fields). As expected, the results are very close between the LR and RRM simulations in  
195 the low-resolution (~100 km) areas (not shown), facilitating our subsequent investigation of the impacts  
196 of regional refinement on the aerosol mass budget and the aerosol forcing over CONUS.



197  
 198 Figure 1. E3SMv1 RRM domain (spectral elements) in (a) an orthographic projection and (b) a cylindrical  
 199 equidistant projection. (a) and (b) show the boundaries of spectral element grids. The red rectangle in (b) outlines  
 200 the region we focus on in the following analyses, referred to as the RRM region.

### 201 **3 Results and Discussions**

202 We focus our analysis on the refined region, as outlined by the red box in Figure 1b (hereafter  
 203 referred to as the RRM region), and the annual mean simulation results in 2016 unless stated otherwise.

204 The LR and RRM simulation results have been regridded to  $1^\circ \times 1^\circ$  to facilitate their comparison unless  
205 otherwise indicated.

### 206 **3.1 Aerosol natural sources**

207 Table 1 summarizes the annual mean sources and burdens of the seven aerosol species in the RRM  
208 region from the LR and RRM simulations. We find the largest relative differences in the sources and mass  
209 burden of the natural wind-driven aerosols between the RRM and LR simulations. With higher horizontal  
210 resolution, the RRM simulation produces more dust (154%), sea salt (13%), and MOM (10%) emissions  
211 than LR. The dust emission enhancement by RRM is concentrated in several inland regions with high  
212 dust emissions, especially in the Mohave and Sonoran deserts (referred to as Region 1) and the northern  
213 North American Prairie (referred to as Region 2) (Figures 2a and 2b). In comparison, the increases in sea  
214 salt and MOM emissions mainly occur around the coastal lines (Figures 2c-2f). That dust emissions  
215 increase with finer model resolutions has been identified in earlier studies (Caldwell et al., 2019; Feng et  
216 al., 2022; Ridley et al., 2013), which attributed the increase to more frequent occurrences of strong winds  
217 in high-resolution simulations. Dust emissions are nonlinearly correlated with surface winds and are  
218 particularly sensitive to strong winds (Zender et al., 2003). We find larger (11.2%) annual mean surface  
219 wind speeds and more frequent strong winds in Region 1 in the RRM simulation compared to the LR  
220 simulation (Figures 3c and 3d), which can explain the dust emission increase in Region 1 under regional  
221 refinement (Figure 2b). However, in Region 2, the annual mean surface wind speeds differ slightly (2.2%)  
222 between the RRM and LR simulations. Besides, the probability density functions (PDFs) of wind speed in  
223 Region 2 are similar between the two simulations (Figures 3c and 3e), as well as the PDFs of friction  
224 velocity (not shown), indicating that surface winds and friction velocities alone cannot explain the dust  
225 emission enhancement in the RRM simulation. In addition to surface winds and friction velocity, soil  
226 moisture can also influence dust emissions by improving the friction velocity threshold (Namikas and  
227 Sherman, 1997; Zender et al., 2003). Therefore, high soil moisture may inhibit saltation and thus reduce

228 dust emissions. We find lower (-7.1%) volumetric soil water content in the surface layer in Region 2 in  
 229 the RRM simulation than in the LR simulation (Figure 3b), which is consistent with the dust emission  
 230 increase in the region by RRM (Figure 2b). The reduced surface soil water content in Region 2 is likely  
 231 related to less precipitation (-3.0%) in the RRM simulation compared to the LR simulation (Figure 4c).

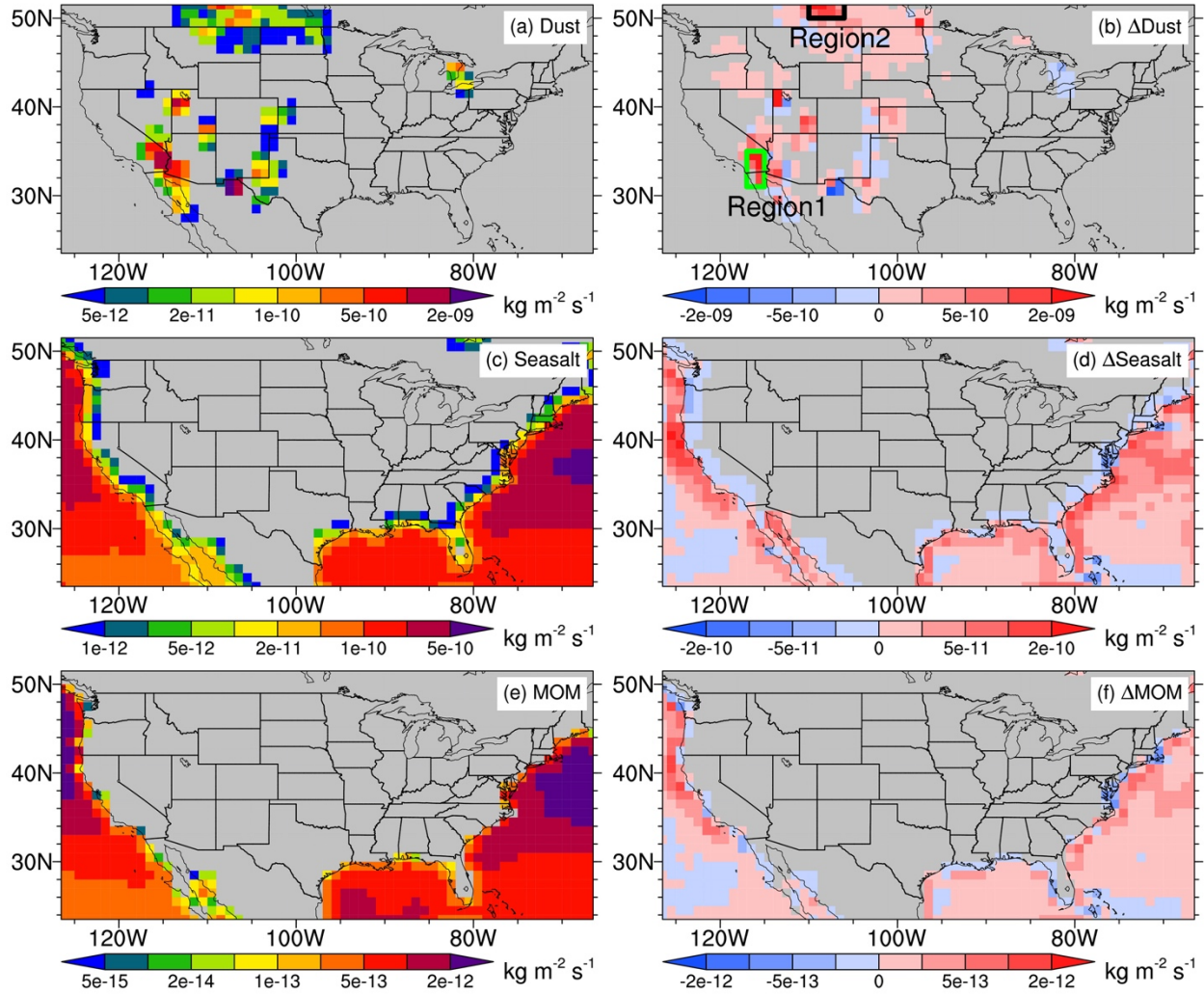
232 **Table 1.** Total annual mean sources and burden in the RRM region for the seven aerosol species

	Sources			Burden		
	RRM / Tg yr <sup>-1</sup>	LR / Tg yr <sup>-1</sup>	Relative diff <sup>1</sup> / %	RRM / Tg	LR / Tg	Relative diff / %
Dust	22.3	8.79	154	0.126	0.0910	39
Sea salt	39.4	34.9	13	0.0875	0.0782	12
MOM	0.192	0.175	10	0.00114	0.00104	9.8
BC	0.268	0.268	0.0030	0.00446	0.00446	-0.050
POM	1.15	1.15	0.022	0.0287	0.0286	0.30
SOA	2.70	2.68	0.72	0.0859	0.0857	0.26
SO <sub>4</sub> <sup>2</sup>	1.74	1.69	2.8	0.0216	0.0215	0.41

233 <sup>1</sup>Relative diff = (RRM/LR - 1) × 100%.

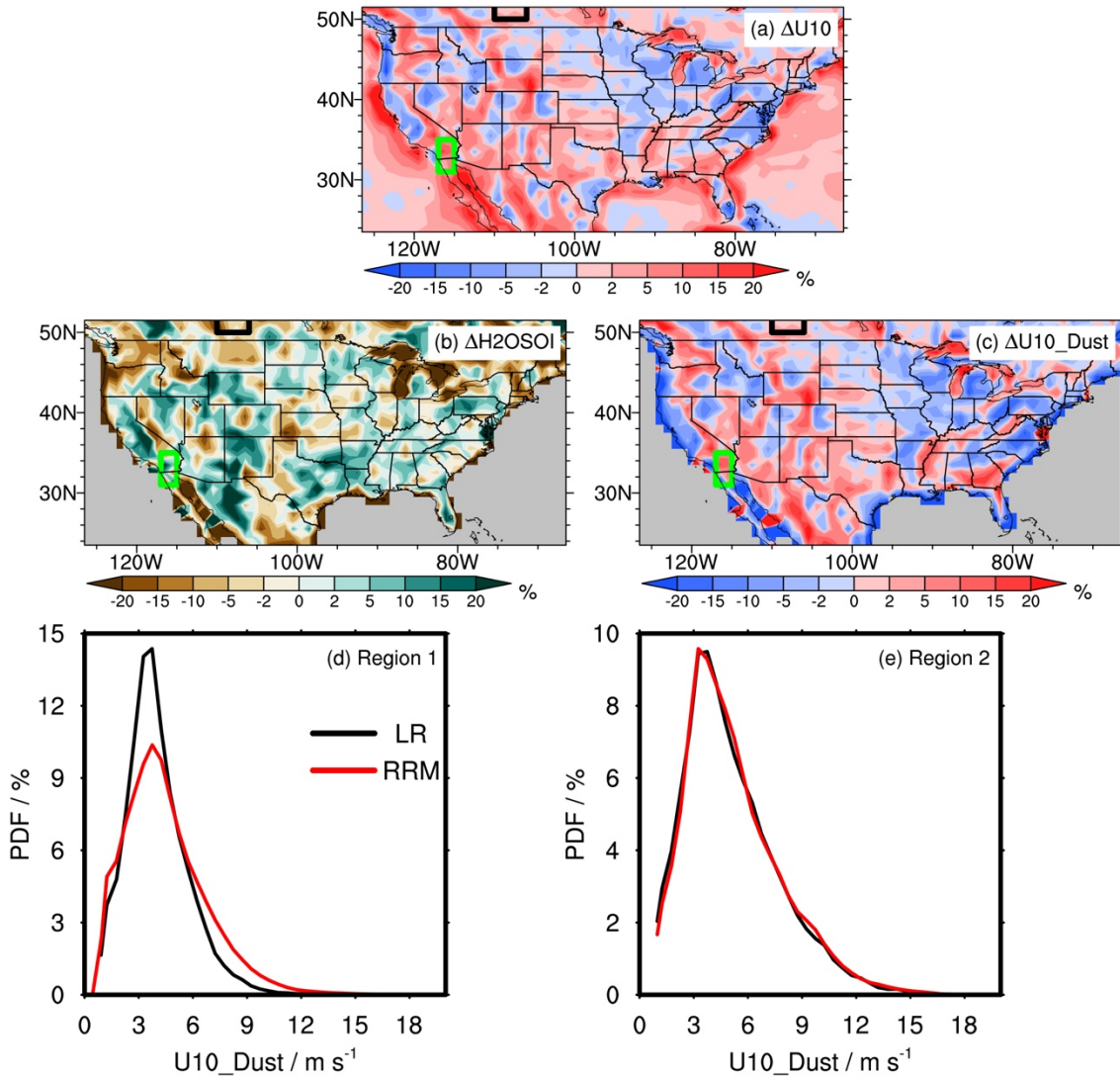
234 <sup>2</sup>SO<sub>4</sub> is represented in the mass of sulfur (TgS y<sup>-1</sup> for sources and TgS for burden). Besides direct anthropogenic  
 235 emissions of SO<sub>4</sub>, other SO<sub>4</sub> sources include gas-aerosol exchange, aqueous-phase production (aqueous-phase  
 236 chemistry and cloud water uptake), and new particle formation.

237 As mentioned above, sea salt and MOM emissions are related to surface wind speed and sea surface  
 238 temperature (Burrows et al., 2022; Liu et al., 2012). We attribute the increased sea salt and MOM  
 239 emissions in the RRM simulation to enhanced surface wind speeds at the finer model resolution, as shown  
 240 in Figure 3a. In addition, since sea salt and MOM are only emitted over the ocean, the distinct land-ocean  
 241 boundaries may also partially contribute to the discrepancies in sea salt and MOM emissions between the  
 242 RRM and LR simulations.



243  
 244 Figure 2. Left column: spatial distributions of annual mean sources of (a) dust, (c) sea salt, and (e) MOM from the  
 245 LR simulation. Right column: the same as the left column but for the absolute differences between the RRM and LR  
 246 simulations (RRM-LR). The green and black boxes in (b) highlight two subregions with substantial changes in dust  
 247 emissions when applying regional refinement. Region 1 is around the Mohave and Sonoran deserts, and Region 2 is  
 248 in the northern North American Prairie.

249



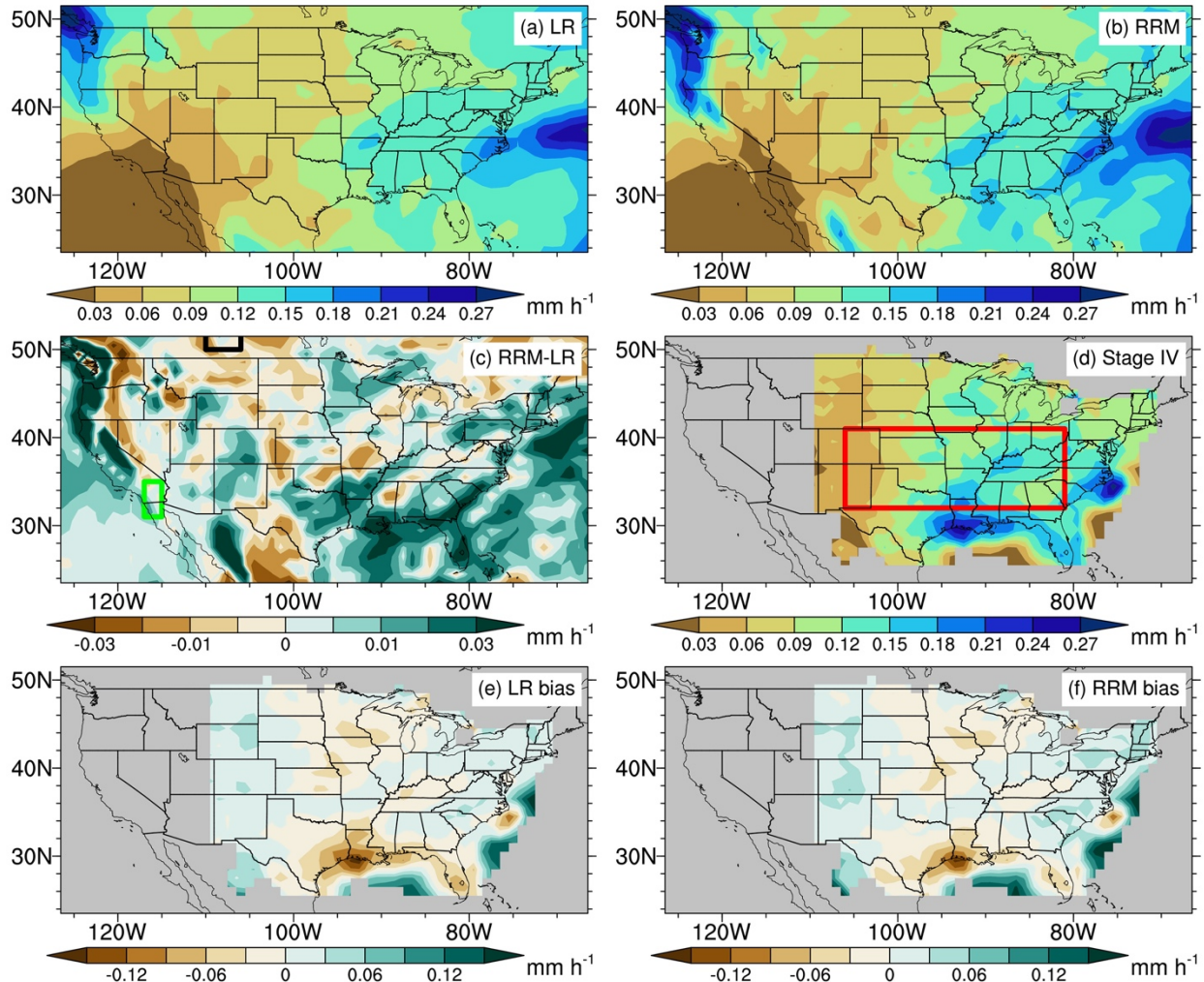
250  
 251 Figure 3. Spatial distributions of the relative differences in annual mean (a) 10-m wind speed from the E3SMv1  
 252 atmospheric component (U10), (b) surface-layer volumetric soil water content (H2OSOI), and (c) 10-m wind speed  
 253 used in the dust emission parameterization (U10\_Dust) between the RRM and LR simulations (RRM-LR). The  
 254 green and black boxes in (a), (b), and (c) are the same as those in Figure 2b. (d, e) Probability density functions  
 255 (PDFs) of U10\_Dust in (d) Region 1 and (e) Region 2. The black lines are for the LR simulation, while the red lines  
 256 are for the RRM simulation. U10\_Dust on native model grids with an output frequency of 15 minutes is used to  
 257 derive the corresponding PDF. Notably, U10\_Dust is slightly different from U10, which considers the convective  
 258 gustiness effect.

## 259 **3.2 Aerosol wet scavenging by convective vs. large-scale precipitation**

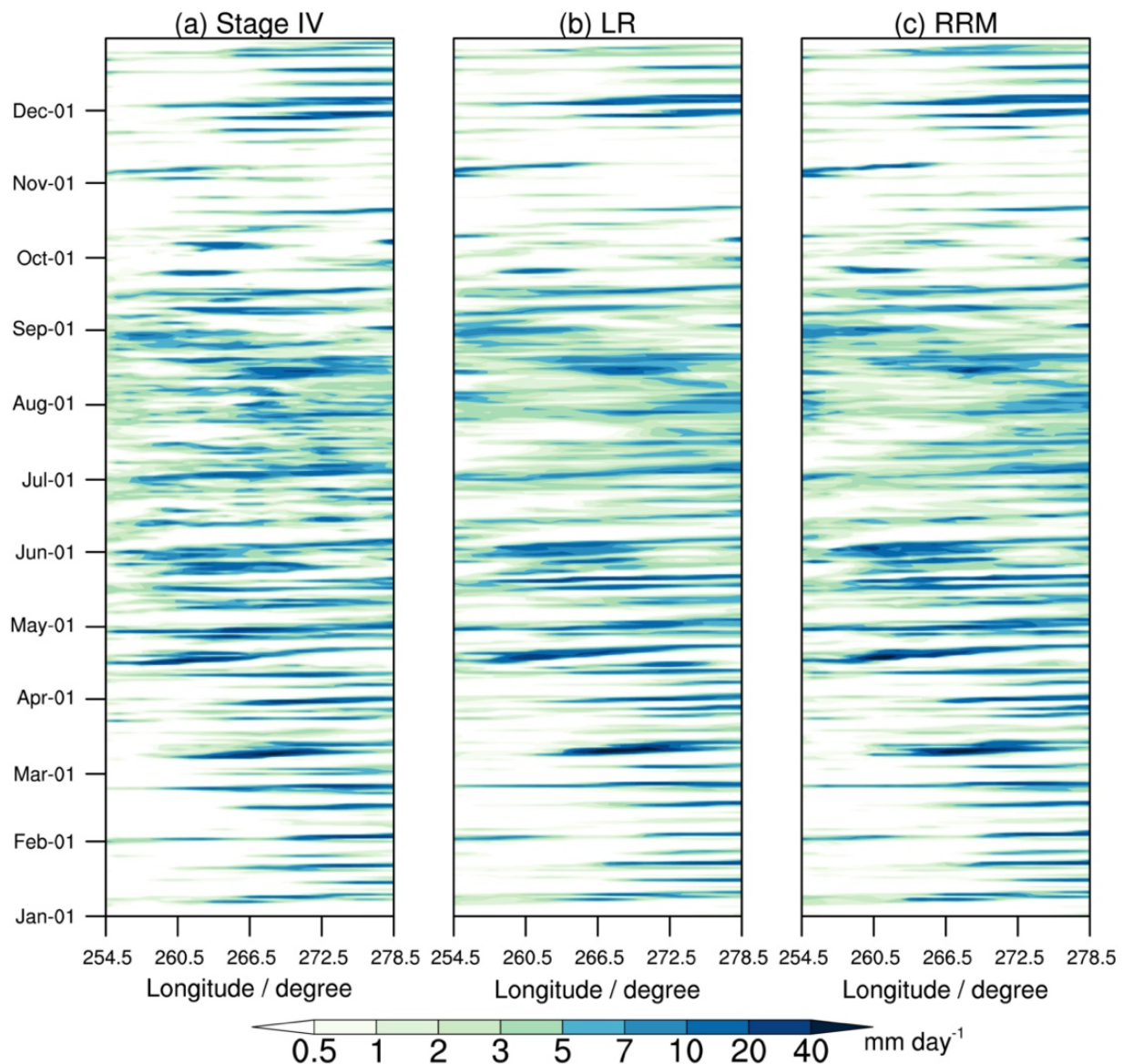
260 In the RRM region, wet scavenging is the primary sink for most aerosol species in both simulations  
261 except for dust and sea salt, the sinks of which are dominated by dry deposition. To understand the impact  
262 of horizontal grid spacing on aerosol wet scavenging, it is necessary first to investigate how precipitation  
263 differs between the LR and RRM simulations.

264 Figure 4 evaluates the LR and RRM simulated precipitation against the observational Stage IV data.  
265 Stage IV is a radar-based precipitation product with rain-gauge bias adjustment and has a native  
266 resolution of 4 km (Lin and Mitchell, 2005). We regrid the Stage IV data to  $1^\circ \times 1^\circ$  for comparison with  
267 our simulation results. Both simulations can capture the observed east-west precipitation gradient in the  
268 US east of the Rocky Mountains. The spatial correlation coefficient between the LR simulation and Stage  
269 IV is 0.52, similar to that between RRM and Stage IV. Moreover, most observed precipitation events in  
270 the central-eastern US (red box in Figure 4d) are well simulated by the LR and RRM simulations  
271 according to the Hovmöller diagrams of meridionally averaged daily precipitation rates in Figure 5, which  
272 is attributed to the appropriate nudging strategy applied to the simulations. However, apparent dry biases  
273 are found near the coastal areas of the southern US in the LR simulation (Figure 4e). By producing more  
274 precipitation than the LR simulation around the US coastal areas, RRM can reduce the dry bias in the  
275 southern coastal regions. However, its precipitation is still much lower than observed (Figure 4f). Minor  
276 dry biases are also found in the northern Great Plains in both simulations. The model dry biases in the  
277 southern and northern Great Plains may be due to the limitation of E3SM in predicting extreme  
278 precipitation events, such as mesoscale convective systems (Feng et al., 2021; Wang et al., 2021), which  
279 is the dominant precipitation contributor in the Great Plains (Li et al., 2021). A noticeable improvement  
280 of the RRM simulation compared to the LR simulation is the production of more frequent heavy  
281 precipitation ( $> 7.6 \text{ mm h}^{-1}$ ), which is mainly attributed to the intensification of large-scale precipitation  
282 (Figure 6), consistent with the results from Caldwell et al. (2019). More frequent heavy precipitation can

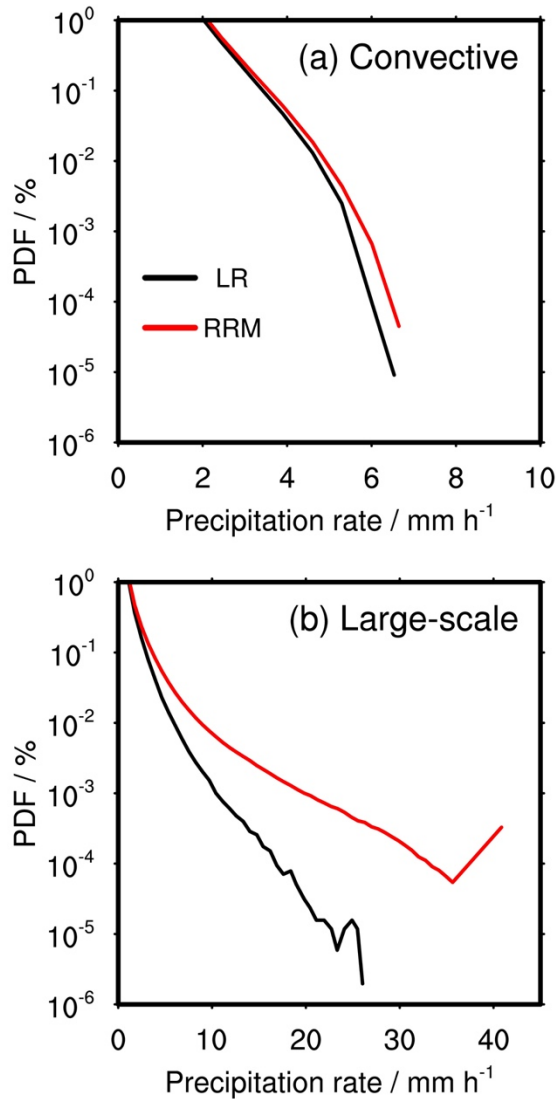
283 partially alleviate the “too frequent, too weak” problem in low-resolution E3SM simulations (Caldwell et al., 2019). However, our result contradicts Tang et al. (2019), which found more light precipitation but less heavy precipitation as model horizontal resolution increases. It may be because Tang et al. (2019) didn’t apply nudging to their low-resolution and RRM simulations, and precipitation varied much between the two simulations.



288  
 289 Figure 4. (a-c) Spatial distributions of annual mean total precipitation rates (large-scale and convective) for the (a)  
 290 LR and (b) RRM simulations and (c) their differences (RRM-LR). The green and black boxes in (c) are the same as  
 291 those in Figure 2b. (d-f) Spatial distributions of annual mean precipitation from Stage IV and the precipitation bias  
 292 of the LR and RRM simulations against Stage IV. The regional mean biases of the LR and RRM simulations are  
 293 0.004 mm h<sup>-1</sup> and 0.010 mm h<sup>-1</sup> compared to Stage IV with a regional mean precipitation of 0.107 mm h<sup>-1</sup>. It  
 294 is noteworthy that the data quality of Stage IV is poor over the open ocean and the western US due to limited radar  
 295 coverage. The Hovmöller diagram in Figure 5 is based on the red box in (d).



296  
 297 Figure 5. Hovmöller diagrams of meridionally averaged daily precipitation rates in the red box of Figure 4d for (a)  
 298 Stage IV, (b) the LR simulation, and (c) the RRM simulation in 2016. The centered pattern correlation coefficient  
 299 between LR and Stage IV is 0.28, the same as that between RRM and Stage IV. The root-mean-square errors of LR  
 300 and RRM are  $5.3 \text{ mm day}^{-1}$  and  $5.5 \text{ mm day}^{-1}$ , respectively, against Stage IV.



301 Figure 6. Probability density functions (PDFs) of (a) convective and (b) large-scale precipitation rates in the RRM  
 302 region for the LR (black lines) and RRM (red lines) simulations. Precipitation on native grids with an output  
 303 frequency of 15 minutes is used to calculate the corresponding PDF.  
 304

305 In addition to affecting total precipitation rates, the model resolution notably changes the partitioning  
 306 between large-scale precipitation (that is computed by the MG2 cloud microphysics parameterization) and  
 307 deep convective precipitation (that is computed by the ZM deep convection parametrization). As model  
 308 resolution increases, more precipitation can be resolved, which leads to an increase in large-scale  
 309 precipitation and a decrease in convective precipitation (Figures 7a and 7b) (Tang et al., 2019).

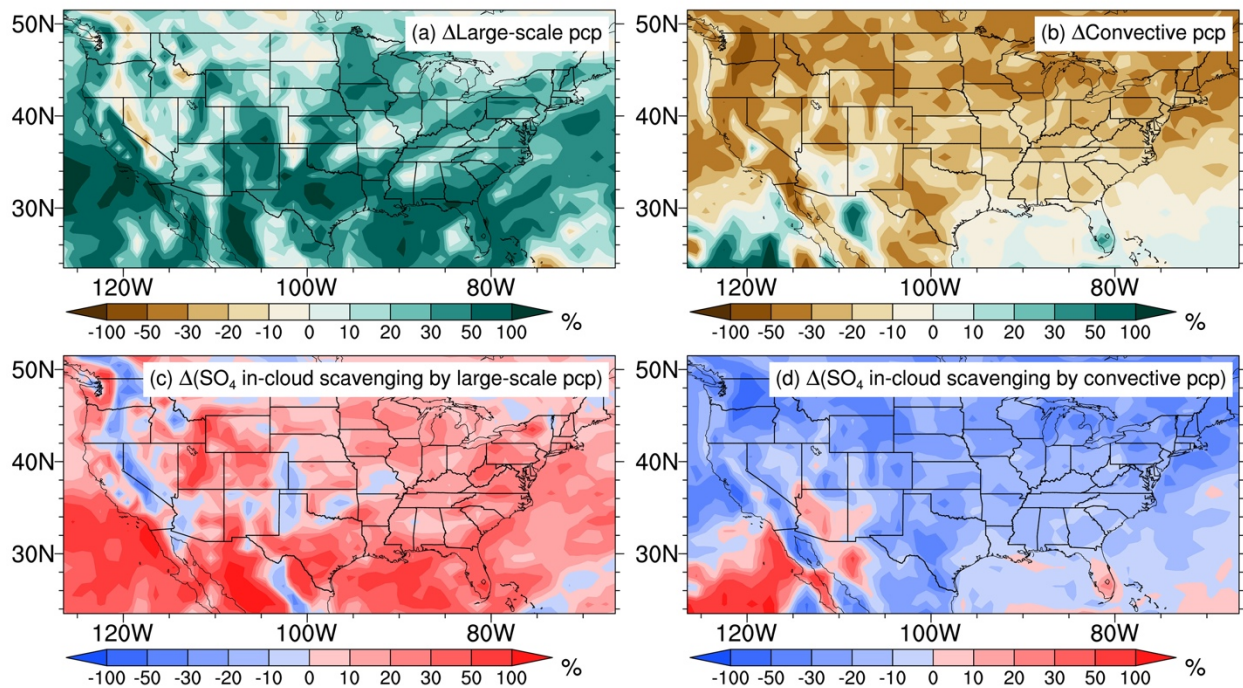
310 In E3SMv1, aerosol wet removal by large-scale and convective precipitation is comprised of in-  
 311 cloud scavenging, which involves the activation of interstitial aerosol particles (IAPs) and the subsequent

312 removal of cloud-borne aerosol by precipitation, and below-cloud scavenging accounting for the removal  
313 of IAPs by precipitation via impaction and Brownian diffusion (Liu et al., 2012; Wang et al., 2013). In-  
314 cloud scavenging is the dominant process for all aerosol species in the RRM region, accounting for ~80%  
315 of the wet removal of sea salt and dust and more than 98% of the other aerosol species.

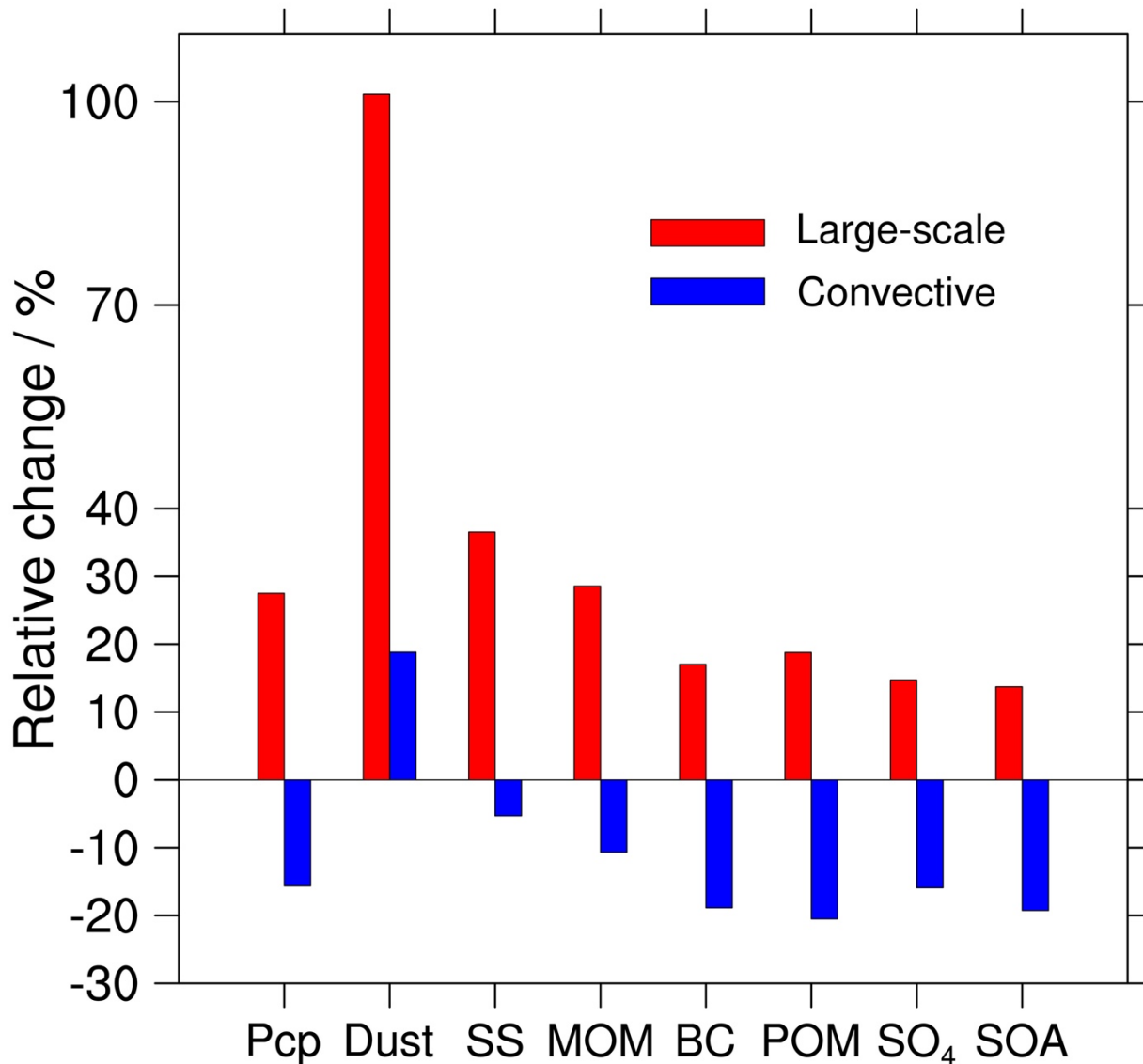
316 EAMv1 uses two different parameterizations to treat aerosol wet scavenging by large-scale clouds  
317 and deep convective clouds. Here, “large-scale clouds” refer to clouds represented by the CLUBB and  
318 MG2 parameterizations, and “deep convective clouds” refer to clouds represented by the ZM deep  
319 convection parameterization. In large-scale clouds, aerosol activation is parameterized as a function of  
320 subgrid vertical velocity ( $W_{sub}$ ), aerosol properties, and environmental conditions (Abdul-Razzak and  
321 Ghan, 2000). The first-order loss rates of aerosol are computed by multiplying a solubility factor by the  
322 first-order loss rate of cloud water, which is computed as a function of cloud fraction, cloud water, and  
323 precipitation production rate profiles (Barth et al., 2000; Rasch et al., 2000). In deep convective clouds,  
324 the cloud-borne aerosol mixing ratios are computed by multiplying interstitial aerosol mixing ratios by  
325 the prescribed convective-cloud activation fractions, which depend on aerosol modes and species to  
326 represent the hygroscopicity (Liu et al., 2012; Wang et al., 2013). The solubility factor is a tunable  
327 parameter, and the model uses different solubility factors for large-scale and deep convective clouds (Liu  
328 et al., 2012; Wang et al., 2013).

329 Therefore, the change in the partitioning between large-scale and deep convective precipitation  
330 should make a difference in aerosol wet removal. Taking  $SO_4$  as an example, Figures 7c and 7d show a  
331 significant increase in in-cloud scavenging of  $SO_4$  by large-scale precipitation but a noticeable decrease  
332 by deep convective precipitation in the RRM simulation compared to the LR simulation. The changing  
333 patterns of in-cloud scavenging by large-scale and deep convective precipitation are consistent with the  
334 changes in the corresponding type of precipitation rates. Figure 8 summarizes the relative differences in  
335 regional mean large-scale and deep convective in-cloud scavenging of different aerosol species in the

336 RRM region between the RRM and LR simulations. Due to the increase in large-scale precipitation (28%)  
 337 and the decrease in deep convective precipitation (-16%) in the RRM region, the large-scale in-cloud  
 338 scavenging increases and the deep convective in-cloud scavenging reduces for all aerosol species but dust  
 339 in the RRM simulation compared to the LR simulation. Dust exhibits a different response because dust  
 340 emission is 154% higher in the RRM simulation than in the LR simulation. With the significant increase  
 341 of dust emission and loading in the atmosphere in the RRM simulation, the wet removal of dust by both  
 342 large-scale and deep convective clouds are higher than that in the LR simulation, even though the deep  
 343 convective precipitation rate is lower.



344 Figure 7. (a, b) Spatial distributions of the relative differences in annual mean (a) large-scale and (b) convective  
 345 precipitation between the RRM and LR simulations. (c-d) same as (a) and (b) but for in-cloud scavenging of SO<sub>4</sub> by  
 346 (c) large-scale and (d) convective precipitation.  
 347



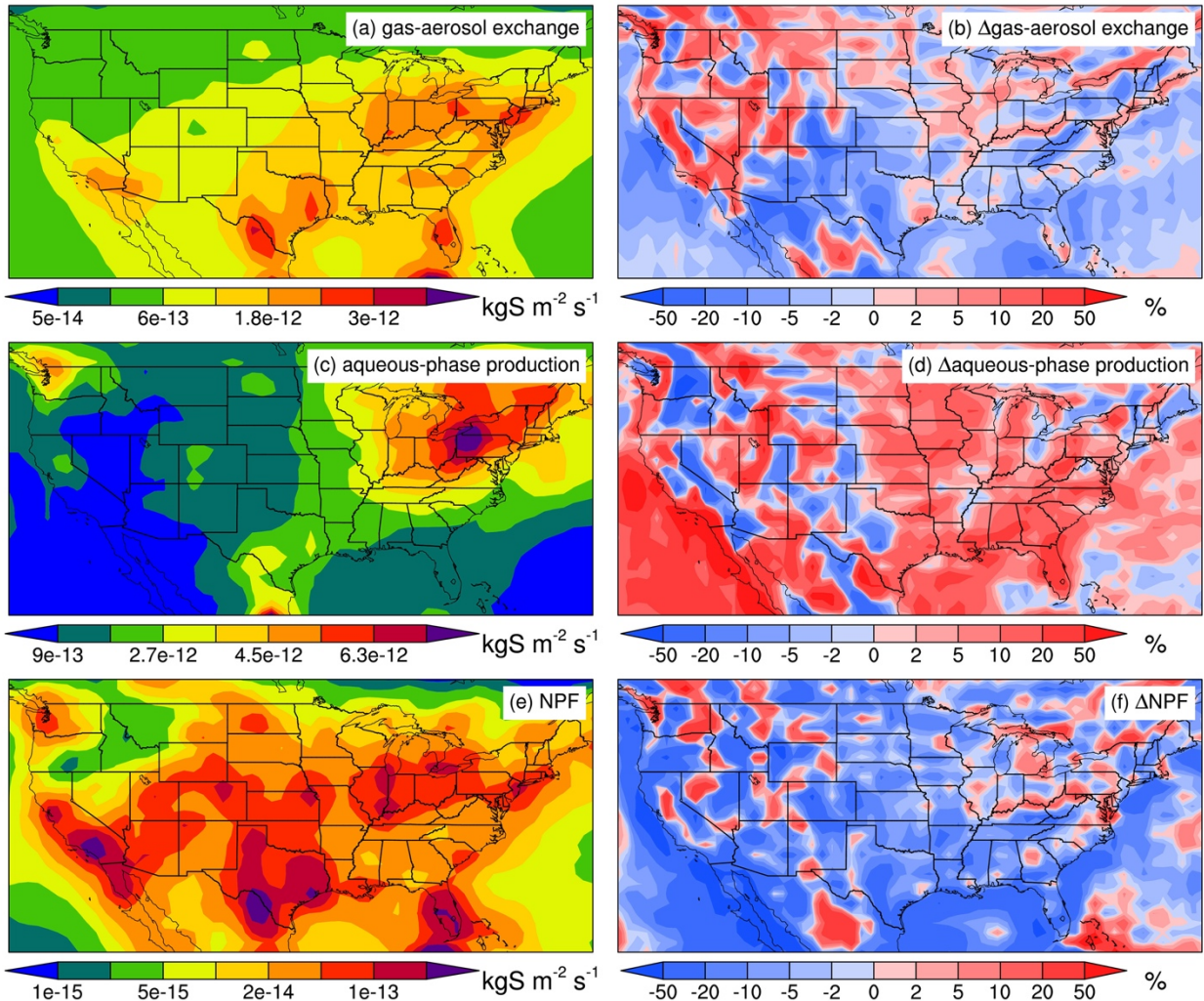
348  
 349 Figure 8. Relative differences in annual regional mean large-scale and convective precipitation and in-cloud  
 350 scavenging of different aerosol species by large-scale and convective precipitation between the RRM and LR  
 351 simulations. “Pcp” refers to precipitation, and “SS” denotes sea salt.

### 352 3.3 Aerosol chemical production

353 As expected, anthropogenic aerosol emissions (e.g., BC, POM, and SOA) prescribed by offline  
 354 emission inventories are almost the same between the RRM and LR simulations. However, the SO<sub>4</sub>  
 355 source in the RRM simulation is 2.8% higher (Table 1). MAM4 considers four source terms for sulfate  
 356 aerosol. Two primary sources of SO<sub>4</sub> are gas-aerosol exchange and aqueous-phase production (Figure  
 357 S3), which contribute to 31% and 63%, respectively, in the RRM region. The other two minor source

358 terms are (1) direct emission of sulfate aerosol and (2) new particle formation (NPF) (Figure S3),  
359 accounting for about 5% and 1% of the total source. Figures 9a and 9c show the spatial distributions of  
360 SO<sub>4</sub> production via the two major pathways from the LR simulation, generally consistent with the  
361 distributions of precursor gases (sulfuric acid gas vapor (H<sub>2</sub>SO<sub>4</sub>) and SO<sub>2</sub> in Figures S4a and S4b) with  
362 one peak in the northeastern US and another peak around southwestern Texas. The RRM simulation  
363 generally produces more SO<sub>4</sub> via aqueous-phase production (6.2% on average over the RRM region) but  
364 less via gas-aerosol exchange (-3.0%) than the LR simulation (Figures 9b and 9d). Figures 9e-9f show  
365 that increasing resolution leads to significantly lower (-13.3%) NPF of SO<sub>4</sub>.

366 SO<sub>4</sub> production via gas-aerosol exchange and NPF positively correlates with the H<sub>2</sub>SO<sub>4</sub>  
367 concentration (Liu et al., 2012). We find a lower (-5.5%) H<sub>2</sub>SO<sub>4</sub> concentration in the RRM than in the LR  
368 (Figure S5a), which can explain the reduction of SO<sub>4</sub> production via gas-aerosol exchange and NPF  
369 (Figure S3). The source of H<sub>2</sub>SO<sub>4</sub> is the oxidation of gas-phase SO<sub>2</sub> by hydroxyl radical (OH) (Figure S3).  
370 In our E3SMv1 configuration, OH concentrations are prescribed, and the reaction rate constants of SO<sub>2</sub>  
371 and OH are similar between the RRM and LR simulations (not shown). Therefore, the H<sub>2</sub>SO<sub>4</sub> production  
372 is dominated by the gas-phase SO<sub>2</sub> concentration, which shows a reduction (-2.3%) in the RRM compared  
373 to the LR (Figure S5b). The sources of gas-phase SO<sub>2</sub> include direct emissions and the oxidation of DMS  
374 by OH and nitrate radical (NO<sub>3</sub>) (Figure S3). DMS and SO<sub>2</sub> emissions are read from emission inventories,  
375 and the reaction rate constants of DMS + OH and DMS + NO<sub>3</sub> are close between the RRM and LR  
376 simulations. Therefore, the gas-phase SO<sub>2</sub> source is similar between the two simulations, and we need to  
377 understand the sinks of gas-phase SO<sub>2</sub> to explain the general reduction of gas-phase SO<sub>2</sub> concentrations in  
378 the RRM simulation.



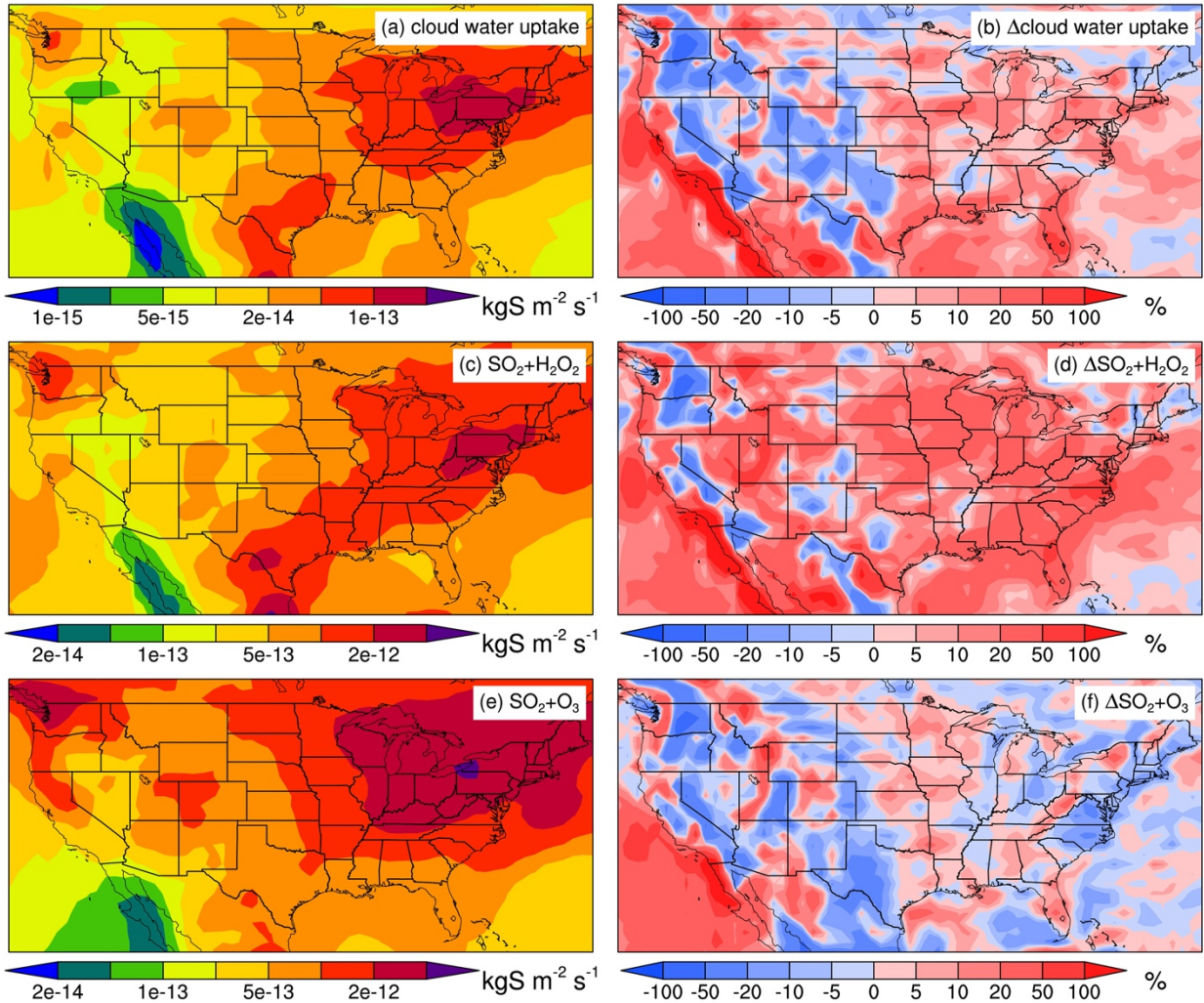
379  
 380 Figure 9. Left column: spatial distributions of annual mean  $\text{SO}_4$  sources from (a) gas-aerosol exchange, (c) aqueous-  
 381 phase production, and (e) NPF in the LR simulation. Right column: the same as the left column but for the relative  
 382 differences between the RRM and LR simulations.

383 We find that dry and wet deposition cannot explain the general reduction of gas-phase  $\text{SO}_2$   
 384 concentrations in the RRM compared to the LR (not shown). Another major sink of gas-phase  $\text{SO}_2$  is the  
 385 oxidation of  $\text{SO}_2$  by hydrogen peroxide ( $\text{H}_2\text{O}_2$ ) and ozone ( $\text{O}_3$ ) to form  $\text{SO}_4$  via aqueous-phase chemistry  
 386 (Figures 10c, 10e, and S3). Another process to produce  $\text{SO}_4$  in the aqueous-phase chemistry module of  
 387 E3SMv1 is the cloud water uptake of  $\text{H}_2\text{SO}_4$  (Figures 10a and S3). All three pathways are related to large-  
 388 scale cloud liquid water content (LWC) (LWC at 700 hPa shown in Figure S4c). The RRM simulation  
 389 generally produces a larger LWC than the LR simulation (700 hPa shown as an example in Figure S5c).  
 390 Therefore, the cloud water uptake of  $\text{H}_2\text{SO}_4$  is enhanced in the RRM simulation (Figures 10b and S3).

391 The aqueous-phase oxidation of  $\text{SO}_2$  by  $\text{H}_2\text{O}_2$  and  $\text{O}_3$  would also be expected to increase with higher  
392 LWC in the RRM simulation. However, we find a slight reduction (-1.2%) in  $\text{SO}_4$  production via the  $\text{O}_3$   
393 pathway (Figure 10f). In contrast, the  $\text{H}_2\text{O}_2$  pathway is enhanced by 17.0% in the RRM simulation  
394 compared to the LR simulation (Figure 10d).

395 The  $\text{H}_2\text{O}_2$  and  $\text{O}_3$  pathways differ in two aspects. First, the  $\text{O}_3$  concentrations are prescribed, while  
396 the  $\text{H}_2\text{O}_2$  concentrations are prognostic in our E3SMv1 configuration (Figures S3 and S4e). Second, the  
397  $\text{O}_3$  pathway is highly sensitive to the pH of the cloud water (proton ( $\text{H}^+$ ) concentrations at 700 hPa shown  
398 in Figure S4d), while the  $\text{H}_2\text{O}_2$  pathway is hardly affected by pH (Seinfeld and Pandis, 2016). We find  
399 that the gas-phase  $\text{H}_2\text{O}_2$  concentrations are generally slightly higher in the RRM than the LR (Figure S5e),  
400 even though the improved  $\text{H}_2\text{O}_2$  pathway should consume more  $\text{H}_2\text{O}_2$  under regional refinement. The  
401 budget analysis (not shown) indicates that the reduction of the gas-phase  $\text{H}_2\text{O}_2$  wet removal in the RRM  
402 simulation contributes to the slightly enhanced  $\text{H}_2\text{O}_2$  concentrations (Figures S3, S4f, and S5f). The  
403 reduced wet removal is related to decreased net rain production (mainly convective) used in the wet  
404 deposition parameterization of gas species (not shown). Notably, the oxidation of  $\text{SO}_2$  by  $\text{H}_2\text{O}_2$  releases  
405  $\text{H}^+$  into cloud water (Figure S3). With increased  $\text{H}_2\text{O}_2$  concentrations, we expect higher  $\text{H}^+$  concentrations  
406 ( $[\text{H}^+]$ ) in large-scale clouds in the RRM simulation than in the LR simulation, as shown in Figure S5d.  
407 Slightly higher  $[\text{H}^+]$  (lower pH) would suppress the aqueous-phase oxidation of  $\text{SO}_2$  by  $\text{O}_3$  significantly  
408 (Seinfeld and Pandis, 2016). These results explain why the  $\text{O}_3$  pathway is suppressed slightly even though  
409 LWC increases in the RRM simulation compared to the LR simulation.

410 In short (Figure S3), higher LWC leads to more  $\text{SO}_4$  production via cloud water uptake and the  
411 aqueous-phase oxidation of  $\text{SO}_2$  by  $\text{H}_2\text{O}_2$ . However, the oxidation of  $\text{SO}_2$  by  $\text{O}_3$  is slightly suppressed due  
412 to the combination of larger LWC and lower pH. Finally, the total aqueous-phase  $\text{SO}_4$  production is  
413 enhanced in the RRM, which consumes more  $\text{SO}_2$  and leads to lower gas-phase  $\text{SO}_2$  concentrations  
414 compared to the LR.

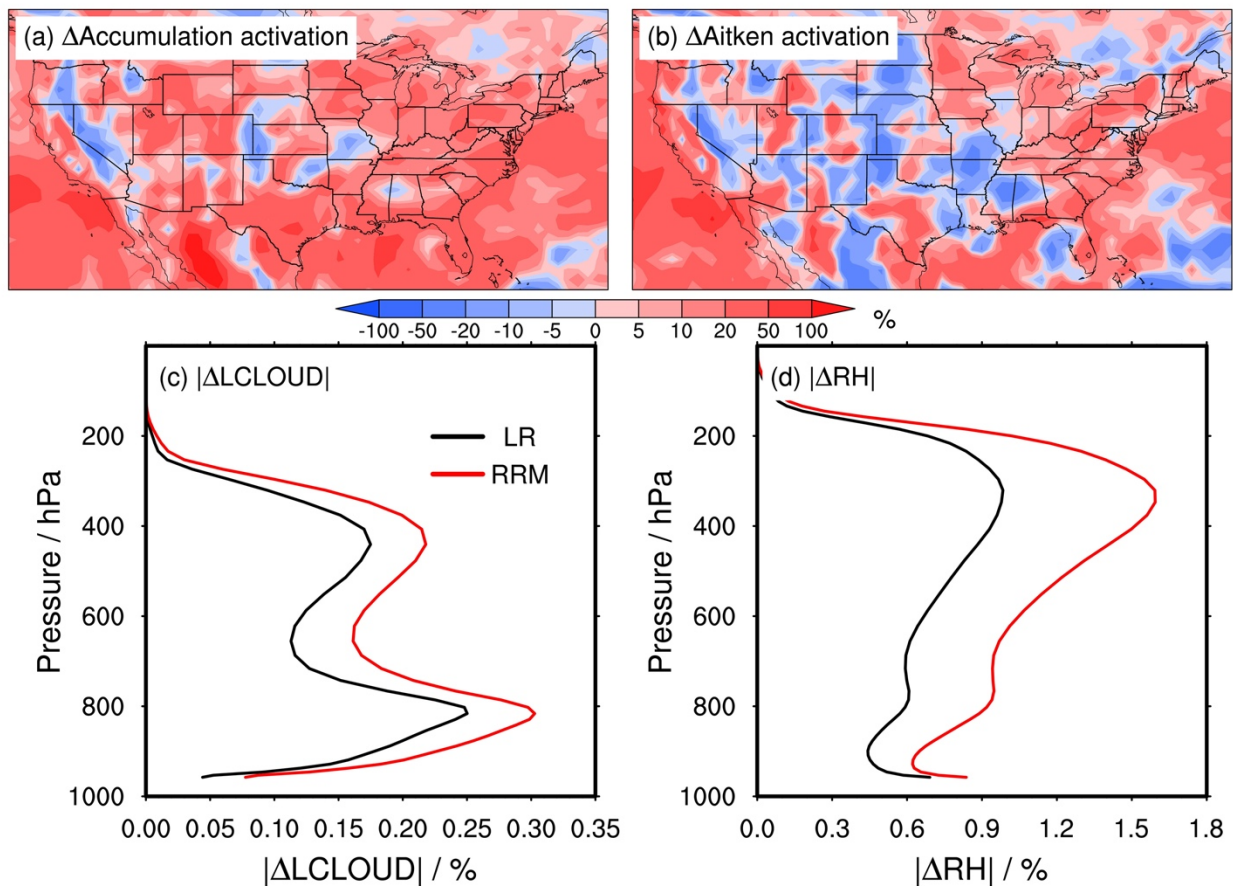


415  
 416 Figure 10. Left column: spatial distributions of annual mean  $\text{SO}_4$  aqueous-phase productions through (a) cloud water  
 417 uptake, (c) the  $\text{H}_2\text{O}_2$  oxidation pathway, and (e) the  $\text{O}_3$  oxidation pathway in the LR simulation. Right column: the  
 418 same as the left column but for the relative differences between the RRM and LR simulations. It is noteworthy that  
 419 the aqueous-phase production occurs in large-scale clouds.

### 420 3.4 Aerosol-cloud interactions

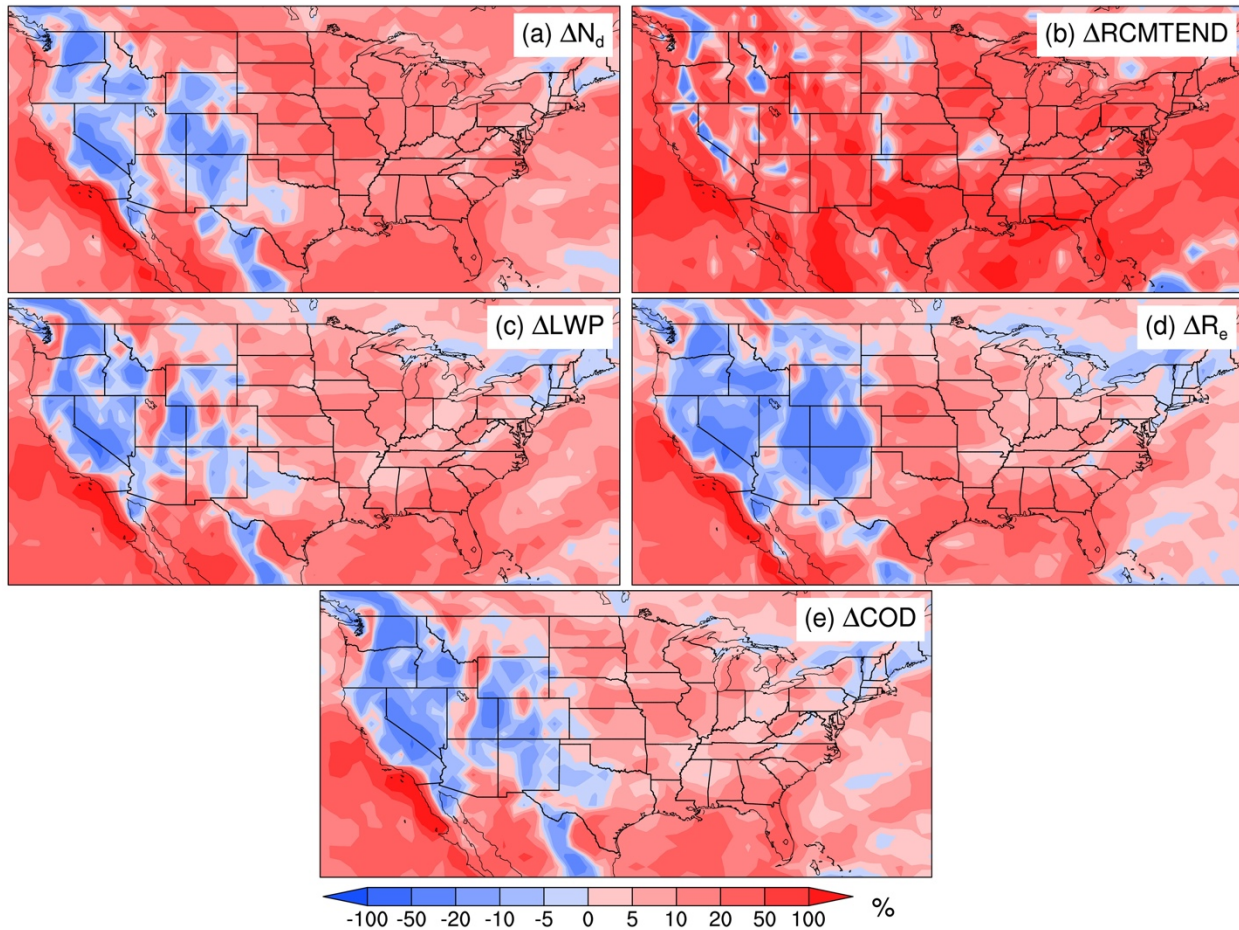
421 Aerosol activation in large-scale clouds is parameterized consistently with droplet nucleation. In  
 422 EAMv1, most IAPs exist in accumulation and Aitken modes (Figures S6a and S6b). We find the aerosol  
 423 activation in the RRM is, on average, enhanced by 13.7% (accumulation mode) and 5.8% (Aitken mode)  
 424 compared to the LR (Figures 11a and 11b). Aerosol activation in large-scale clouds primarily occurs in  
 425 two pathways. One is related to cloud expansion (i.e., increase in cloud fraction, which leads to aerosol  
 426 activation) and shrinkage (i.e., decrease in cloud fraction, which leads to aerosol resuspension) in the

427 same grid box (hereafter referred to as the cloud-intermittency pathway) between model timesteps. The  
428 other refers to the activation of IAPs that are brought to the cloud base by updrafts (hereafter referred to  
429 as the updraft pathway) (Liu et al., 2012). We find that the cloud-intermittency pathway contributes to  
430 almost all the aerosol activation enhancement in Aitken mode but only about half of the enhancement in  
431 accumulation mode under regional refinement (not shown). The updraft pathway accounts for the other  
432 half of the enhancement in accumulation mode. The contrast RRM impacts on the updraft pathway  
433 between the accumulation and Aitken modes may be related to the distinct vertical profiles of IAPs from  
434 the two modes (Figure S6c). The cloud-intermittency pathway is parameterized as a function of  $W_{sub}$ ,  
435 aerosol properties, and the change of large-scale liquid cloud fractions between two consecutive time  
436 steps ( $\Delta L C L O U D$ ) (Abdul-Razzak and Ghan, 2000; Zhang et al., 2022a). Positive  $\Delta L C L O U D$   
437 corresponds to cloud expansion, and negative  $\Delta L C L O U D$  denotes cloud shrinkage. We do not find any  
438 noticeable differences in  $W_{sub}$  and aerosol properties between the RRM and LR simulations. However,  
439  $|\Delta L C L O U D|$  is considerably larger in the RRM, which indicates larger L C L O U D temporal variability  
440 (Figure 11c), resulting in increased microphysical cloud processing of aerosols and more aerosol  
441 activation via the cloud-intermittency pathway. The larger L C L O U D temporal variability is consistent  
442 with the larger relative humidity (RH) temporal variability in the RRM than in the LR (Figure 11d)  
443 (Golaz et al., 2002).



444 Figure 11. (a, b) Spatial distributions of the relative differences in the annual mean vertical-integrated IAP activation  
 445 fluxes in large-scale clouds for (a) accumulation and (b) Aitken modes between the RRM and LR simulations. (c)  
 446 Vertical profiles of the annual regional mean absolute temporal variabilities of large-scale liquid cloud fractions  
 447 ( $|\Delta L CLOUD|$ ).  $|\Delta L CLOUD| = |L CLOUD_{t_2} - L CLOUD_{t_1}|$ ;  $t_2$  and  $t_1$  indicate two consecutive model time steps. The  
 448 red line indicates the RRM simulation and the black line for the LR simulation. (d) the same as (c) but for relative  
 449 humidity (RH).  
 450

451 Enhanced aerosol activation results in higher droplet number concentrations ( $N_d$ ) in the RRM  
 452 compared to the LR (Figure 12a). Moreover, the CLUBB vertical-integrated cloud liquid water tendency  
 453 (RCMTEND), which is dominated by water vapor condensation, is generally remarkably larger in the  
 454 RRM simulation (Figure 12b), which leads to higher large-scale cloud liquid water path (LWP) and LWC  
 455 (Figures 12c and S5c). Larger RCMTEND may also contribute to larger droplets at the cloud top in the  
 456 RRM simulation ( $R_e$  in Figure 12d;  $R_e$  — grid-cell mean droplet effective radius at the top of liquid water  
 457 clouds), even though  $N_d$  increases. With higher LWP and larger  $R_e$ , cloud optical depth (COD) is also  
 458 higher (Figure 12e).



459  
 460 Figure 12. Spatial distributions of the relative differences in annual mean (a) grid-cell mean vertical-integrated  
 461 droplet number concentrations ( $N_d$ ), (b) CLUBB vertical-integrated cloud liquid water tendency (RCMTEND), (c)  
 462 grid-cell mean liquid water path (LWP), (d) grid-cell mean droplet effective radius at the top of liquid water clouds  
 463 ( $R_e$ ), and (e) grid-cell mean cloud optical path (COD) between the RRM and LR simulations. It is noteworthy that  
 464  $N_d$ , RCMTEND, LWP, and  $R_e$  are exclusively for large-scale clouds, while COD considers both large-scale and  
 465 convective clouds but is dominated by large-scale (not shown). The spatial distributions of  $N_d$ , RCMTEND,  
 466 LWP,  $R_e$ , and COD from the LR simulation are shown in Figure S7.

### 467 3.5 Anthropogenic aerosol effective radiative forcing

468 With considerable impacts on cloud properties, the regional refinement should also influence  $ERF_{aer}$ .

469 We use the Ghan (2013) method to decompose  $ERF_{aer}$  into direct, indirect, and surface albedo effects.

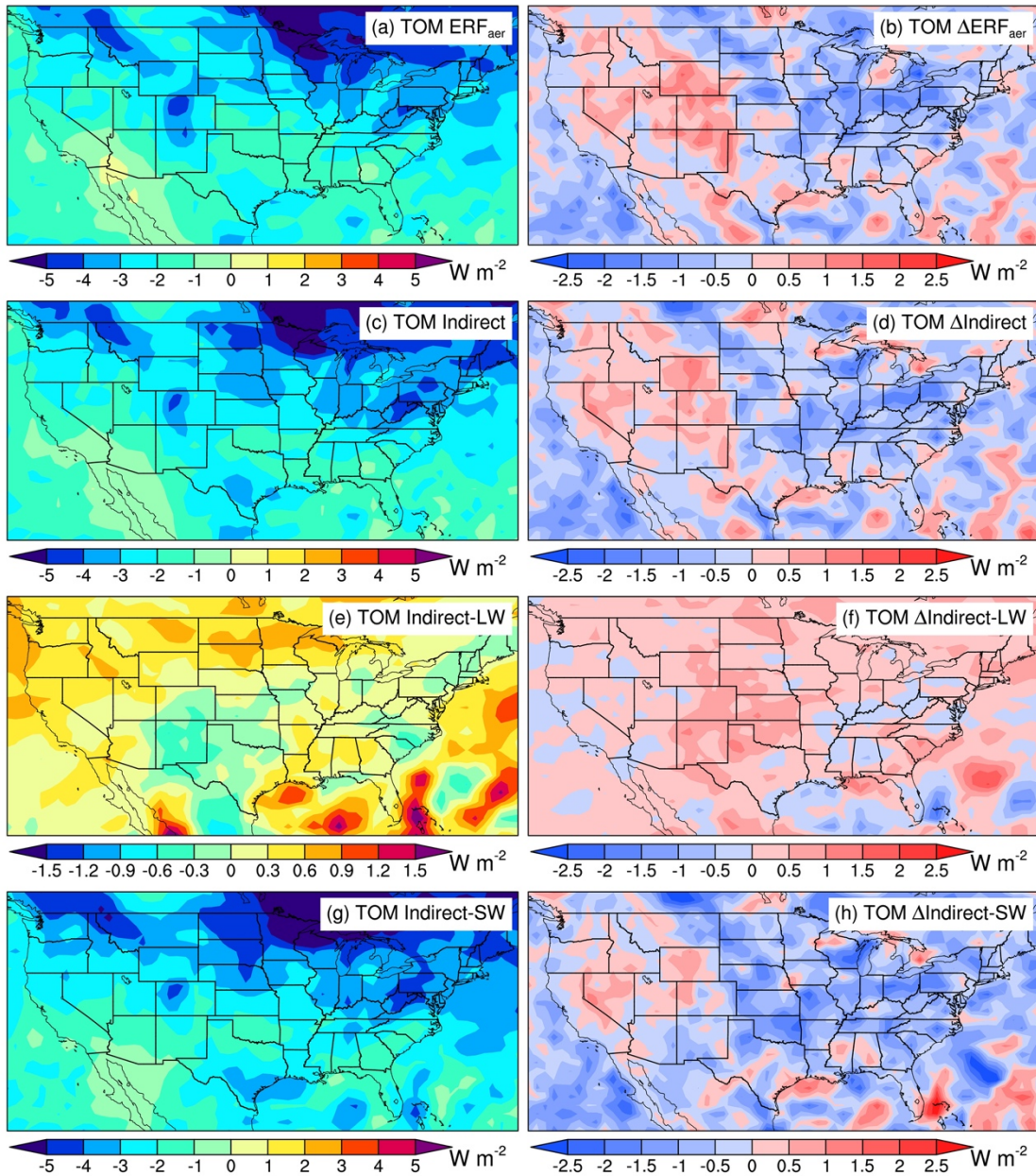
470 Figure 13 shows a stronger (more negative) anthropogenic aerosol shortwave indirect effect ( $-0.52 \text{ W m}^{-2}$ )

471 and enhanced longwave indirect effect ( $0.21 \text{ W m}^{-2}$ ) at the top of the model (TOM) in the RRM

472 simulation compared to the LR simulation. The net (shortwave + longwave) indirect effect is  $0.31 \text{ W m}^{-2}$

473 more negative in the RRM simulation compared to the LR simulation, which is about a 12%

474 enhancement. The total  $ERF_{aer}$  at TOM is  $0.27 \text{ W m}^{-2}$  more negative in the RRM simulation, about a 12%  
 475 enhancement compared to the LR simulation. We also find that the RRM simulation produces a 10%  
 476 enhancement of  $ERF_{aer}$  at the surface (Figure S8).



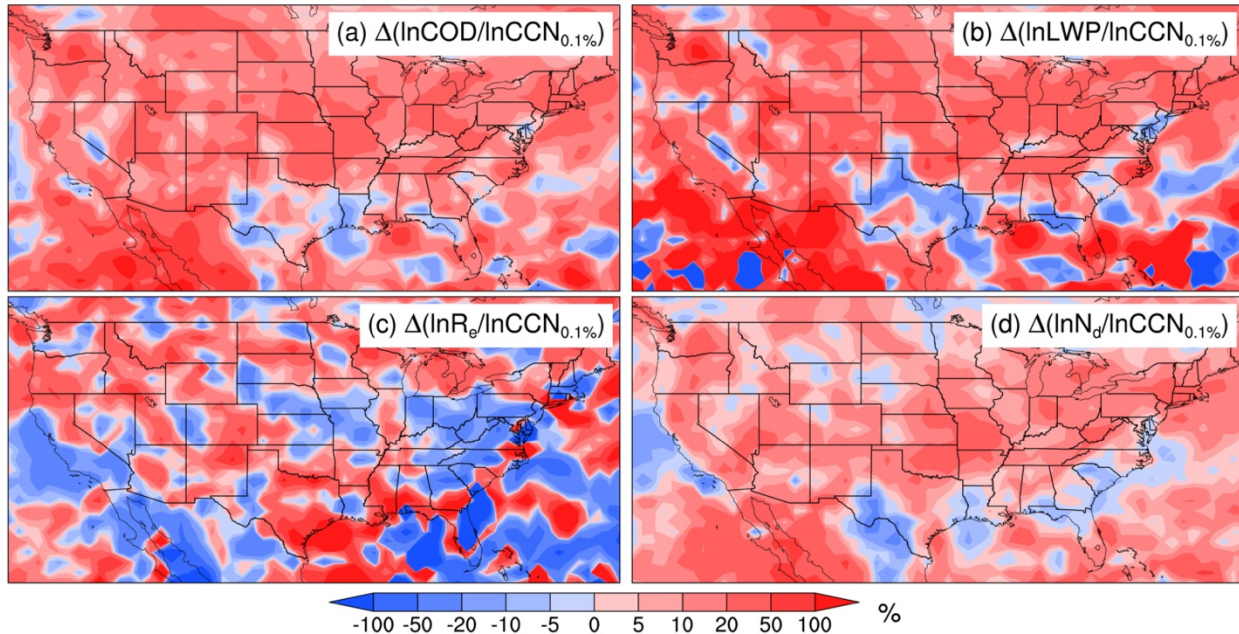
477  
 478 Figure 13. (a) Spatial distribution of annual mean  $ERF_{aer}$  at the top of the model (TOM) from the LR simulation. (c,  
 479 e, g) Same as (a) but for  $ERF_{aer}$  attributed to (c) aerosol indirect effect (longwave + shortwave), (e) aerosol  
 480 longwave indirect effect, and (g) aerosol shortwave indirect effect. The right column is the same as the left but for  
 481 the absolute differences between the RRM and LR simulations.

482 To understand the enhancement of  $ERF_{aer}$  in the RRM experiment, we compare the production  
483 efficiencies of  $N_d$ ,  $R_e$ , LWP, and COD due to anthropogenic aerosols between the RRM and LR  
484 simulations (Figure 14). In Figure 14, the relative changes of  $N_d$ , LWP, and COD per relative change of  
485 CCN at 0.1% supersaturation ( $CCN_{0.1\%}$ ) between the PD and PI simulations are generally larger in the  
486 RRM simulation, consistent with our earlier analysis of the enhanced aerosol activation in RRM. Because  
487 cloud properties are more sensitive to anthropogenic aerosols in the RRM, the RRM configuration  
488 produces stronger anthropogenic-aerosol-cloud interactions and  $ERF_{aer}$  (Figure 13).

489 This result differs from Ma et al. (2015), which demonstrated that higher model resolutions would  
490 weaken the aerosol indirect effect. Ma et al. (2015) identified the increased droplet nucleation in  
491 simulations with higher resolutions, leading to a stronger first aerosol indirect effect, which is consistent  
492 with this study. However, their LWP response to anthropogenic aerosols weakens (lower LWP) as  
493 resolution increases, leading to reduced second aerosol indirect effect, in contrast to the larger LWP  
494 production efficiencies in our RRM simulation (Figure 14b). The discrepancies may be caused by  
495 different parameterizations of water vapor condensation to form cloud liquid water. The water vapor  
496 condensation is parameterized in CLUBB on the basis of joint PDFs of vertical velocity, temperature, and  
497 moisture in our simulations (Golaz et al., 2002), while it was calculated in CAM5 in Ma et al. (2015)  
498 using a saturation equilibrium adjustment approach (Park et al., 2014). The water vapor condensation  
499 parameterization affects not only LWP but also the subsequent aqueous-phase chemistry calculation  
500 discussed in Section 3.3. Therefore, it is necessary to evaluate the sensitivity of water vapor condensation  
501 to model resolutions when different parametrizations are used, as their resolution sensitivity can be very  
502 different.

503 Our finding regarding the stronger aerosol indirect effect as resolution increases is also different  
504 from Caldwell et al. (2019), which found that the aerosol indirect effect changed only slightly from the  
505 low-resolution to high-resolution simulations. This discrepancy might be attributed to the fact that the  
506 model timesteps used in low- and high-resolution model simulations are very different in Caldwell et al.

507 (2019) but are kept the same in this study. Since model timestep can affect model aerosol and clouds,  
 508 aerosol indirect effects can be affected.



509  
 510 Figure 14. Spatial distributions of the relative differences in (a)  $\frac{\ln \text{COD}}{\ln \text{CCN}_{0.1\%}}$ , (b)  $\frac{\ln \text{LWP}}{\ln \text{CCN}_{0.1\%}}$ , (c)  $\frac{\ln R_e}{\ln \text{CCN}_{0.1\%}}$ , and (d)  
 511  $\frac{\ln N_d}{\ln \text{CCN}_{0.1\%}}$  between the RRM and LR simulations. Here,  $\ln x$  denotes the relative change of  $x$  between the PD and PI  
 512 simulations, i.e.,  $\ln x = \frac{PD_x - PI_x}{PI_x}$ . Therefore,  $\frac{\ln x}{\ln \text{CCN}_{0.1\%}}$  reflects the production efficiency of  $x$  by anthropogenic  
 513 aerosols.

## 514 4 Conclusions

515 We investigate the impact of increasing model horizontal resolution on the aerosol mass budget and  
 516  $\text{ERF}_{\text{aer}}$  over the CONUS in 2016 by comparing E3SMv1 LR and RRM simulations (Tables 1 and 2). The  
 517 RRM simulation produces more dust, sea salt, and MOM emissions than the LR simulation due to larger  
 518 surface wind speeds, more frequent strong surface winds, or drier soil. Besides influencing the natural  
 519 aerosol sources, RRM also affects  $\text{SO}_4$  production from gas-aerosol exchange, aqueous-phase chemistry,  
 520 and NPF (Table 2). The reduced  $\text{SO}_4$  production from gas-aerosol exchange and NPF by RRM is due to  
 521 decreased gas-phase  $\text{SO}_2$  and  $\text{H}_2\text{SO}_4$  concentrations in the RRM simulation. Enhanced aqueous-phase  $\text{SO}_4$   
 522 production consumes more  $\text{SO}_2$  under regional refinement, leading to lower gas-phase  $\text{SO}_2$

523 concentrations. The improved aqueous-phase SO<sub>4</sub> production is attributed to more cloud water uptake of  
 524 H<sub>2</sub>SO<sub>4</sub> and more oxidation of SO<sub>2</sub> by H<sub>2</sub>O<sub>2</sub> in large-scale clouds with higher LWC in the RRM  
 525 simulation. In contrast, the oxidation of SO<sub>2</sub> by O<sub>3</sub> is slightly suppressed due to the lower pH of large-  
 526 scale clouds in the RRM simulation compared to the LR simulation, which is a consequence of slightly  
 527 increased gas-phase H<sub>2</sub>O<sub>2</sub> concentrations releasing more H<sup>+</sup> through the oxidation of SO<sub>2</sub> by H<sub>2</sub>O<sub>2</sub>.

528 **Table 2.** Comparison of aerosol-relevant properties in the RRM region between the LR and RRM  
 529 simulations

		RRM	LR	Relative diff <sup>1</sup> / %
Precipitation / mm day <sup>-1</sup>	Large-scale	1.55	1.21	27.5
	Convective	1.00	1.18	-15.6
SO <sub>4</sub> in-cloud scavenging / TgS yr <sup>-1</sup>	Large-scale precipitation	0.982	0.856	14.7
	Convective precipitation	0.356	0.424	-15.9
	Gas-aerosol exchange	0.515	0.531	-3.0
SO <sub>4</sub> production / TgS yr <sup>-1</sup>	Aqueous-phase production	1.13	1.06	6.2
	NPF	0.0182	0.0210	-13.3
Aerosol activation / 10 <sup>5</sup> m <sup>-2</sup> s <sup>-1</sup>	Aitken mode	10.09	8.87	13.7
	Accumulation mode	2.22	2.09	5.8
N <sub>d</sub> / 10 <sup>10</sup> m <sup>-2</sup>		1.30	1.17	11.5
R <sub>c</sub> / μm		1.56	1.45	7.7
LWP / g m <sup>-2</sup>		33.0	30.7	7.3
COD		5.14	4.86	5.6
TOM ERF <sub>aer</sub> / W m <sup>-2</sup>	Indirect shortwave	-3.27	-2.74	19.1
	Indirect longwave	0.50	0.29	72.0
	Total indirect	-2.76	-2.45	12.8
	Total (indirect + direct + albedo)	-2.66	-2.38	11.5

530 <sup>1</sup>Relative diff = (RRM/LR - 1) × 100%.

531 Increasing model horizontal resolution affects the partitioning between large-scale and convective  
 532 precipitation (Table 2). With more resolved large-scale precipitation and less parameterized deep

533 convective precipitation, in-cloud scavenging of aerosols by large-scale (deep convective) precipitation  
534 generally increases (decreases) in the RRM simulation compared to the LR simulation.

535 RRM enhances the activation of IAPs in large-scale clouds due to the larger temporal variability of  
536 LSCLOUD in the RRM simulation compared to the LR simulation (Table 2). Enhanced aerosol activation  
537 leads to more cloud droplets. In addition, RRM enhances water vapor condensation, resulting in larger  
538 LWP and  $R_e$ , which leads to larger COD. Since aerosol activation is stronger in the RRM simulation,  
539 cloud droplets, LWP, and COD are more sensitive to anthropogenic aerosols. Consequently, the  
540 anthropogenic aerosol indirect effect and  $ERF_{aer}$  in the RRM are stronger than in the LR simulation (Table  
541 2).

542 Although the study is limited to comparing the E3SMv1 LR (~100 km) and CONUS RRM (~25 km)  
543 simulations, the methodology shown in the study is helpful for future studies to investigate the potential  
544 impacts of model resolutions on the simulation results, as RRM is significantly less expensive  
545 computationally compared to the global high-resolution model. Some findings from this study may also  
546 apply to E3SM simulations at higher resolutions or even convection-permitting scales, such as the  
547 enhancement in natural aerosol emissions due to stronger winds, the partitioning between large-scale and  
548 convective precipitation and associated wet scavenging, and improved IAP activation in large-scale  
549 clouds. However, we must also emphasize that the aerosol mass budget and  $ERF_{aer}$  are sensitive to model  
550 configurations and regional characteristics such as aerosol properties, land use and land cover, and  
551 climate. Aerosol and clouds in other regions can be very different. Furthermore, some resolution  
552 sensitivities may differ as model resolution advances to convection-permitting and subgrid-scale  
553 processes become more significant. Moreover, although nudging is applied in the study to minimize the  
554 impacts of large-scale circulations on aerosol properties as horizontal resolution changes, differences in  
555 meteorology still exist between the RRM and LR simulations (e.g., surface wind speed and precipitation).  
556 Therefore, the results above contain the meteorological effect, although the meteorological differences are  
557 also caused by the change in horizontal grid spacing.



559 **Code availability**

560 The E3SMv1 source code is available at <https://doi.org/10.11578/E3SM/dc.20180418.36> (E3SM  
561 Project, 2018) (last access: April 11, 2022).

562

563 **Data availability**

564 We use the Stage IV precipitation data from the MCS-IDC data product, available at  
565 <http://dx.doi.org/10.25584/1632005> (Li et al., 2020). The LR and RRM simulation results are available at  
566 <https://doi.org/10.5281/zenodo.7782985> (Li et al., 2023). The level-3 Moderate Resolution Imaging  
567 Spectroradiometer (MODIS) gridded ( $1^\circ \times 1^\circ$ ) monthly Dark Target aerosol optical depth (AOD)  
568 products used in the supplement are from [https://doi.org/10.5067/MODIS/MOD08\\_M3.061](https://doi.org/10.5067/MODIS/MOD08_M3.061)  
569 (MOD08\_M3; last access: Nov 28, 2023) and [https://doi.org/10.5067/MODIS/MYD08\\_M3.061](https://doi.org/10.5067/MODIS/MYD08_M3.061)  
570 (MYD08\_M3; last access: Nov 28, 2023). The Aerosol Robotic Network (AERONET) data is available at  
571 [https://aeronet.gsfc.nasa.gov/new\\_web/download\\_all\\_v3\\_aod.html](https://aeronet.gsfc.nasa.gov/new_web/download_all_v3_aod.html) (last access: May 26, 2022). The  
572 Interagency Monitoring of Protected Visual Environments (IMPROVE) data is available at  
573 <https://views.cira.colostate.edu/fed/QueryWizard/> (last access: May 26, 2022).

574

575 **Author contributions**

576 KZ and JL designed the study. JL conducted the simulations under the instructions of KZ and with  
577 the help of TH, BS, and QY. KZ and SZ determined the nudging strategy, and JL prepared the ERA5  
578 nudging files under the instructions of SZ and KZ. JL performed the analyses with discussions with KZ,  
579 TH, PM, and HH. JL prepared the paper with contributions from all coauthors.

580 **Competing Interests**

581 Po-Lun Ma is a Topical Editor of Geoscientific Model Development. Other authors declare that they  
582 have no conflict of interest.

583

## 584 **Acknowledgments**

585       The study was supported as part of the Enabling Aerosol–cloud interactions at GLObal convection-  
586 permitting scales (EAGLES) project (project no. 74358) sponsored by the United States Department of  
587 Energy (DOE), Office of Science, Office of Biological and Environmental Research, Earth System Model  
588 Development (ESMD) program area. The Pacific Northwest National Laboratory (PNNL) is operated for  
589 the DOE by the Battelle Memorial Institute under Contract DE-AC05-76RL01830. The research used  
590 high-performance computing resources from the PNNL Research Computing and resources of the  
591 National Energy Research Scientific Computing Center (NERSC), a U.S. Department of Energy Office of  
592 Science User Facility located at Lawrence Berkeley National Laboratory, operated under Contract No.  
593 DE-AC02-05CH11231 using NERSC awards ALCC-ERCAP0016315, BER-ERCAP0015329, BER-  
594 ERCAP0018473, and BER-ERCAP0020990. IMPROVE is a collaborative association of state, tribal, and  
595 federal agencies, and international partners. US Environmental Protection Agency is the primary funding  
596 source, with contracting and research support from the National Park Service. The Air Quality Group at  
597 the University of California, Davis is the central analytical laboratory, with ion analysis provided by  
598 Research Triangle Institute, and carbon analysis provided by Desert Research Institute. We thank Ilya  
599 Slutsker and many other Principal Investigators (PIs) or co-PIs and their staff for establishing and  
600 maintaining the AERONET sites used in the study.

601

## 602 References

- 603 Abdul - Razzak, H., and Ghan, S. J.: A parameterization of aerosol activation: 2. Multiple aerosol types, *J. Geophys.*  
604 *Res.-Atmos.*, 105, 6837-6844, <https://doi.org/10.1029/1999JD901161>, 2000.
- 605 Apte, J. S., Marshall, J. D., Cohen, A. J., and Brauer, M.: Addressing global mortality from ambient PM<sub>2.5</sub>, *Environ.*  
606 *Sci. Technol.*, 49, 8057-8066, <https://doi.org/10.1021/acs.est.5b01236>, 2015.
- 607 Barth, M., Rasch, P., Kiehl, J., Benkovitz, C., and Schwartz, S.: Sulfur chemistry in the National Center for  
608 Atmospheric Research Community Climate Model: Description, evaluation, features, and sensitivity to aqueous  
609 chemistry, *J. Geophys. Res.-Atmos.*, 105, 1387-1415, <https://doi.org/10.1029/1999JD900773>, 2000.
- 610 Bogenschütz, P. A., Gettelman, A., Morrison, H., Larson, V. E., Craig, C., and Schanen, D. P.: Higher-order  
611 turbulence closure and its impact on climate simulations in the Community Atmosphere Model, *J. Clim.*, 26, 9655-  
612 9676, <https://doi.org/10.1175/JCLI-D-13-00075.1>, 2013.
- 613 Burrows, S. M., Easter, R. C., Liu, X., Ma, P.-L., Wang, H., Elliott, S. M., Singh, B., Zhang, K., and Rasch, P. J.:  
614 OCEANFILMS (Organic Compounds from Ecosystems to Aerosols: Natural Films and Interfaces via Langmuir  
615 Molecular Surfactants) sea spray organic aerosol emissions—implementation in a global climate model and impacts  
616 on clouds, *Atmos. Chem. Phys.*, 22, 5223-5251, <https://doi.org/10.5194/acp-22-5223-2022>, 2022.
- 617 Caldwell, P. M., Mamejtanov, A., Tang, Q., Van Roekel, L. P., Golaz, J. C., Lin, W., Bader, D. C., Keen, N. D.,  
618 Feng, Y., and Jacob, R.: The DOE E3SM coupled model version 1: Description and results at high resolution,  
619 *Journal of Advances in Modeling Earth Systems*, 11, 4095-4146, <https://doi.org/10.1029/2019MS001870>, 2019.
- 620 Caldwell, P. M., Terai, C. R., Hillman, B., Keen, N. D., Bogenschütz, P., Lin, W., Beydoun, H., Taylor, M.,  
621 Bertagna, L., and Bradley, A.: Convection - permitting simulations with the E3SM global atmosphere model,  
622 *Journal of Advances in Modeling Earth Systems*, 13, e2021MS002544, <https://doi.org/10.1029/2021MS002544>,  
623 2021.
- 624 Dennis, J. M., Edwards, J., Evans, K. J., Guba, O., Lauritzen, P. H., Mirin, A. A., St-Cyr, A., Taylor, M. A., and  
625 Worley, P. H.: CAM-SE: A scalable spectral element dynamical core for the Community Atmosphere Model, *The*  
626 *International Journal of High Performance Computing Applications*, 26, 74-89,  
627 <https://doi.org/10.1177/1094342011428142>, 2012.
- 628 Dueben, P. D., Wedi, N., Saarinen, S., and Zeman, C.: Global simulations of the atmosphere at 1.45 km grid-spacing  
629 with the Integrated Forecasting System, *Journal of the Meteorological Society of Japan. Ser. II*, 98, 551-572,  
630 <https://doi.org/10.2151/jmsj.2020-016>, 2020.
- 631 E3SM Project, DOE: Energy Exascale Earth System Model v1.0, [code],  
632 <https://doi.org/10.11578/E3SM/dc.20180418.36>, 2018.
- 633 Feng, L., Smith, S. J., Braun, C., Crippa, M., Gidden, M. J., Hoesly, R., Klimont, Z., Van Marle, M., Van Den Berg,  
634 M., and Van Der Werf, G. R.: The generation of gridded emissions data for CMIP6, *Geoscientific Model*  
635 *Development*, 13, 461-482, <https://doi.org/10.5194/gmd-13-461-2020>, 2020.
- 636 Feng, Y., Wang, H., Rasch, P., Zhang, K., Lin, W., Tang, Q., Xie, S., Hamilton, D., Mahowald, N., and Yu, H.:  
637 Global dust cycle and direct radiative effect in E3SM version 1: Impact of increasing model resolution, *Journal of*  
638 *Advances in Modeling Earth Systems*, 14, e2021MS002909, <https://doi.org/10.1029/2021MS002909>, 2022.

639 Feng, Z., Song, F., Sakaguchi, K., and Leung, L. R.: Evaluation of Mesoscale Convective Systems in Climate  
640 Simulations: Methodological Development and Results from MPAS-CAM over the United States, *J. Clim.*, 34,  
641 2611-2633, <https://doi.org/10.1175/JCLI-D-20-0136.1>, 2021.

642 Ghan, S. J.: Estimating aerosol effects on cloud radiative forcing, *Atmos. Chem. Phys.*, 13, 9971-9974,  
643 <https://doi.org/10.5194/acp-13-9971-2013>, 2013.

644 Golaz, J.-C., Larson, V. E., and Cotton, W. R.: A PDF-based model for boundary layer clouds. Part I: Method and  
645 model description, *Journal of the atmospheric sciences*, 59, 3540-3551, [https://doi.org/10.1175/1520-0469\(2002\)059<3540:APBMFB>2.0.CO;2](https://doi.org/10.1175/1520-0469(2002)059<3540:APBMFB>2.0.CO;2), 2002.

647 Golaz, J.-C., Van Roekel, L. P., Zheng, X., Roberts, A. F., Wolfe, J. D., Lin, W., Bradley, A. M., Tang, Q., Maltrud,  
648 M. E., and Forsyth, R. M.: The DOE E3SM Model Version 2: overview of the physical model and initial model  
649 evaluation, *Journal of Advances in Modeling Earth Systems*, 14, <https://doi.org/10.1029/2022MS003156>, 2022.

650 Golaz, J. C., Caldwell, P. M., Van Roekel, L. P., Petersen, M. R., Tang, Q., Wolfe, J. D., Abeshu, G., Anantharaj,  
651 V., Asay - Davis, X. S., and Bader, D. C.: The DOE E3SM coupled model version 1: Overview and evaluation at  
652 standard resolution, *Journal of Advances in Modeling Earth Systems*, 11, 2089-2129,  
653 <https://doi.org/10.1029/2018MS001603>, 2019.

654 Hamilton, D. S., Perron, M. M., Bond, T. C., Bowie, A. R., Buchholz, R. R., Guieu, C., Ito, A., Maenhaut, W.,  
655 Myriokefalitakis, S., and Olgun, N.: Earth, wind, fire, and pollution: Aerosol nutrient sources and impacts on ocean  
656 biogeochemistry, *Annual Review of Marine Science*, 14, 303-330, <https://doi.org/10.1146/annurev-marine-031921-013612>, 2022.

658 Harris, L. M., Lin, S.-J., and Tu, C.: High-resolution climate simulations using GFDL HiRAM with a stretched  
659 global grid, *J. Clim.*, 29, 4293-4314, <https://doi.org/10.1175/JCLI-D-15-0389.1>, 2016.

660 Heinzeller, D., Duda, M. G., and Kunstmann, H.: Towards convection-resolving, global atmospheric simulations  
661 with the Model for Prediction Across Scales (MPAS) v3.1: An extreme scaling experiment, *Geoscientific Model  
662 Development*, 9, 77-110, <https://doi.org/10.5194/gmd-9-77-2016>, 2016.

663 Hersbach, H., Bell, B., Berrisford, P., Hirahara, S., Horányi, A., Muñoz - Sabater, J., Nicolas, J., Peubey, C., Radu,  
664 R., and Schepers, D.: The ERA5 global reanalysis, *Quarterly Journal of the Royal Meteorological Society*, 146,  
665 1999-2049, <https://doi.org/10.1002/qj.3803>, 2020.

666 Hoesly, R. M., Smith, S. J., Feng, L., Klimont, Z., Janssens-Maenhout, G., Pitkanen, T., Seibert, J. J., Vu, L.,  
667 Andres, R. J., and Bolt, R. M.: Historical (1750–2014) anthropogenic emissions of reactive gases and aerosols from  
668 the Community Emissions Data System (CEDs), *Geoscientific Model Development*, 11, 369-408,  
669 <https://doi.org/10.5194/gmd-11-369-2018>, 2018.

670 Hoose, C., Kristjánsson, J. E., Chen, J.-P., and Hazra, A.: A classical-theory-based parameterization of  
671 heterogeneous ice nucleation by mineral dust, soot, and biological particles in a global climate model, *Journal of the  
672 Atmospheric Sciences*, 67, 2483-2503, <https://doi.org/10.1175/2010JAS3425.1>, 2010.

673 Hurrell, J. W., Hack, J. J., Shea, D., Caron, J. M., and Rosinski, J.: A new sea surface temperature and sea ice  
674 boundary dataset for the Community Atmosphere Model, *J. Clim.*, 21, 5145-5153,  
675 <https://doi.org/10.1175/2008JCLI2292.1>, 2008.

676 Iacono, M. J., Delamere, J. S., Mlawer, E. J., Shephard, M. W., Clough, S. A., and Collins, W. D.: Radiative forcing  
677 by long - lived greenhouse gases: Calculations with the AER radiative transfer models, *J. Geophys. Res.-Atmos.*,  
678 113, <https://doi.org/10.1029/2008JD009944>, 2008.

679 Jickells, T., An, Z., Andersen, K. K., Baker, A., Bergametti, G., Brooks, N., Cao, J., Boyd, P., Duce, R., and Hunter,  
680 K.: Global iron connections between desert dust, ocean biogeochemistry, and climate, *Science*, 308, 67-71,  
681 <https://doi.org/10.1126/science.1105959>, 2005.

682 Kooperman, G. J., Pritchard, M. S., Ghan, S. J., Wang, M., Somerville, R. C., and Russell, L. M.: Constraining the  
683 influence of natural variability to improve estimates of global aerosol indirect effects in a nudged version of the  
684 Community Atmosphere Model 5, *J. Geophys. Res.-Atmos.*, 117, <https://doi.org/10.1029/2012JD018588>, 2012.

685 Larson, V. E., Golaz, J.-C., and Cotton, W. R.: Small-scale and mesoscale variability in cloudy boundary layers:  
686 Joint probability density functions, *Journal of the atmospheric sciences*, 59, 3519-3539,  
687 [https://doi.org/10.1175/1520-0469\(2002\)059<3519:SSAMVI>2.0.CO;2](https://doi.org/10.1175/1520-0469(2002)059<3519:SSAMVI>2.0.CO;2), 2002.

688 Li, J., Han, X., Jin, M., Zhang, X., and Wang, S.: Globally analysing spatiotemporal trends of anthropogenic PM<sub>2.5</sub>  
689 concentration and population's PM<sub>2.5</sub> exposure from 1998 to 2016, *Environ. Int.*, 128, 46-62,  
690 <https://doi.org/10.1016/j.envint.2019.04.026>, 2019.

691 Li, J., Feng, Z., Qian, Y., and Leung, L. R.: MCSs and IDC in the US for 2004 – 2017,  
692 <http://dx.doi.org/10.25584/1632005>, 2020 (last access: June 18, 2020).

693 Li, J., Feng, Z., Qian, Y., and Leung, L. R.: A high-resolution unified observational data product of mesoscale  
694 convective systems and isolated deep convection in the United States for 2004–2017, *Earth Syst. Sci. Data*, 13, 827-  
695 856, <https://doi.org/10.5194/essd-13-827-2021>, 2021.

696 Li, J., Zhang, K., Hassan, T., Zhang, S., Ma, P.-L., Singh, B., Yan, Q., and Huang, H.: Assessing the Sensitivity of  
697 Aerosol Mass Budget and Effective Radiative Forcing to Horizontal Grid Spacing in E3SMv1 Using A Regional  
698 Refinement Approach - E3SM LR and RRM simulation data, <https://doi.org/10.5281/zenodo.7782985>, 2023 (last  
699 access: March 29, 2023).

700 Lim, C.-H., Ryu, J., Choi, Y., Jeon, S. W., and Lee, W.-K.: Understanding global PM<sub>2.5</sub> concentrations and their  
701 drivers in recent decades (1998–2016), *Environ. Int.*, 144, 106011, <https://doi.org/10.1016/j.envint.2020.106011>,  
702 2020.

703 Lin, Y., and Mitchell, K. E.: the NCEP stage II/IV hourly precipitation analyses: Development and applications,  
704 19th Conf. Hydrology, American Meteorological Society, San Diego, CA, USA, 2005,

705 Liu, X., Easter, R. C., Ghan, S. J., Zaveri, R., Rasch, P., Shi, X., Lamarque, J.-F., Gettelman, A., Morrison, H., and  
706 Vitt, F.: Toward a minimal representation of aerosols in climate models: Description and evaluation in the  
707 Community Atmosphere Model CAM5, *Geoscientific Model Development*, 5, 709-739,  
708 <https://doi.org/10.5194/gmd-5-709-2012>, 2012.

709 Liu, X., Ma, P. L., Wang, H., Tilmes, S., Singh, B., Easter, R. C., Ghan, S. J., and Rasch, P. J.: Description and  
710 evaluation of a new four-mode version of the Modal Aerosol Module (MAM4) within version 5.3 of the Community  
711 Atmosphere Model, *Geosci. Model Dev.*, 9, 505-522, <https://doi.org/10.5194/gmd-9-505-2016>, 2016.

712 Ma, P.-L., Rasch, P. J., Fast, J. D., Easter, R. C., Gustafson Jr, W., Liu, X., Ghan, S. J., and Singh, B.: Assessing the  
713 CAM5 physics suite in the WRF-Chem model: Implementation, resolution sensitivity, and a first evaluation for a  
714 regional case study, *Geoscientific Model Development*, 7, 755-778, <https://doi.org/10.5194/gmd-7-755-2014>, 2014.

715 Ma, P. L., Rasch, P. J., Wang, M., Wang, H., Ghan, S. J., Easter, R. C., Gustafson Jr, W. I., Liu, X., Zhang, Y., and  
716 Ma, H. Y.: How does increasing horizontal resolution in a global climate model improve the simulation of aerosol -  
717 cloud interactions?, *Geophys. Res. Lett.*, 42, 5058-5065, <https://doi.org/10.1002/2015GL064183>, 2015.

- 718 Mahowald, N. M., Scanza, R., Brahney, J., Goodale, C. L., Hess, P. G., Moore, J. K., and Neff, J.: Aerosol  
719 deposition impacts on land and ocean carbon cycles, *Current Climate Change Reports*, 3, 16-31,  
720 <https://doi.org/10.1007/s40641-017-0056-z>, 2017.
- 721 Mlawer, E. J., Taubman, S. J., Brown, P. D., Iacono, M. J., and Clough, S. A.: Radiative transfer for inhomogeneous  
722 atmospheres: RRTM, a validated correlated - k model for the longwave, *J. Geophys. Res.-Atmos.*, 102, 16663-  
723 16682, <https://doi.org/10.1029/97JD00237>, 1997.
- 724 Morrison, H., and Gettelman, A.: A new two-moment bulk stratiform cloud microphysics scheme in the Community  
725 Atmosphere Model, version 3 (CAM3). Part I: Description and numerical tests, *J. Clim.*, 21, 3642-3659,  
726 <https://doi.org/10.1175/2008JCLI2105.1>, 2008.
- 727 Namikas, S., and Sherman, D. J.: Predicting aeolian sand transport: Revisiting the White model, *Earth Surface*  
728 *Processes and Landforms: The Journal of the British Geomorphological Group*, 22, 601-604,  
729 [https://doi.org/10.1002/\(SICI\)1096-9837\(199706\)22:6<601::AID-ESP783>3.0.CO;2-5](https://doi.org/10.1002/(SICI)1096-9837(199706)22:6<601::AID-ESP783>3.0.CO;2-5), 1997.
- 730 Neale, R. B., Richter, J. H., and Jochum, M.: The impact of convection on ENSO: From a delayed oscillator to a  
731 series of events, *J. Clim.*, 21, 5904-5924, <https://doi.org/10.1175/2008JCLI2244.1>, 2008.
- 732 Oleson, K. W., Lawrence, D. M., Bonan, G. B., Drewniak, B., Huang, M., Koven, C. D., Levis, S., Li, F., Riley, W.  
733 J., Subin, Z. M., Swenson, S. C., Thornton, P. E., Bozbiyik, A., Fisher, R., Heald, C. L., Kluzek, E., Lamarque, J.-F.,  
734 Lawrence, P. J., Leung, L. R., Lipscomb, W., Muszala, S., Ricciuto, D. M., Sacks, W., Sun, Y., Tang, J., and Yang,  
735 Z.-L.: Technical Description of version 4.5 of the Community Land Model (CLM), available at  
736 <http://dx.doi.org/10.5065/D6RR1W7M>, National Center for Atmospheric Research, Boulder, Colorado, US, 434,  
737 2013.
- 738 Park, S., Bretherton, C. S., and Rasch, P. J.: Integrating cloud processes in the Community Atmosphere Model,  
739 version 5, *J. Clim.*, 27, 6821-6856, <https://doi.org/10.1175/JCLI-D-14-00087.1>, 2014.
- 740 Perring, A., Pusede, S., and Cohen, R.: An observational perspective on the atmospheric impacts of alkyl and  
741 multifunctional nitrates on ozone and secondary organic aerosol, *Chem. Rev.*, 113, 5848-5870,  
742 <https://doi.org/10.1021/cr300520x>, 2013.
- 743 Pusede, S. E., Steiner, A. L., and Cohen, R. C.: Temperature and recent trends in the chemistry of continental  
744 surface ozone, *Chem. Rev.*, 115, 3898-3918, <https://doi.org/10.1021/cr5006815>, 2015.
- 745 Qian, Y., Yasunari, T. J., Doherty, S. J., Flanner, M. G., Lau, W. K., Ming, J., Wang, H., Wang, M., Warren, S. G.,  
746 and Zhang, R.: Light-absorbing particles in snow and ice: Measurement and modeling of climatic and hydrological  
747 impact, *Advances in Atmospheric Sciences*, 32, 64-91, <https://doi.org/10.1007/s00376-014-0010-0>, 2015.
- 748 Rasch, P., Feichter, J., Law, K., Mahowald, N., Penner, J., Benkovitz, C., Genthon, C., Giannakopoulos, C.,  
749 Kasibhatla, P., and Koch, D.: A comparison of scavenging and deposition processes in global models: results from  
750 the WCRP Cambridge Workshop of 1995, *Tellus B*, 52, 1025-1056, <https://doi.org/10.1034/j.1600-0889.2000.00980.x>, 2000.
- 752 Rasch, P., Xie, S., Ma, P. L., Lin, W., Wang, H., Tang, Q., Burrows, S., Caldwell, P., Zhang, K., and Easter, R.: An  
753 overview of the atmospheric component of the Energy Exascale Earth System Model, *Journal of Advances in*  
754 *Modeling Earth Systems*, 11, 2377-2411, <https://doi.org/10.1029/2019MS001629>, 2019.
- 755 Ridley, D. A., Heald, C. L., Pierce, J., and Evans, M.: Toward resolution - independent dust emissions in global  
756 models: Impacts on the seasonal and spatial distribution of dust, *Geophys. Res. Lett.*, 40, 2873-2877,  
757 <https://doi.org/10.1002/grl.50409>, 2013.

- 758 Schwartz, C. S.: Medium-range convection-allowing ensemble forecasts with a variable-resolution global model,  
759 *Monthly Weather Review*, 147, 2997-3023, <https://doi.org/10.1175/MWR-D-18-0452.1>, 2019.
- 760 Seinfeld, J. H., and Pandis, S. N.: Atmospheric chemistry and physics: from air pollution to climate change, John  
761 Wiley & Sons, Inc, Hoboken, New Jersey, 2016.
- 762 Shrivastava, M., Easter, R. C., Liu, X., Zelenyuk, A., Singh, B., Zhang, K., Ma, P. L., Chand, D., Ghan, S., and  
763 Jimenez, J. L.: Global transformation and fate of SOA: Implications of low - volatility SOA and gas - phase  
764 fragmentation reactions, *J. Geophys. Res.-Atmos.*, 120, 4169-4195, <https://doi.org/10.1002/2014JD022563>, 2015.
- 765 Smith, C. J., Kramer, R. J., Myhre, G., Alterskjær, K., Collins, W., Sima, A., Boucher, O., Dufresne, J.-L., Nabat,  
766 P., and Michou, M.: Effective radiative forcing and adjustments in CMIP6 models, *Atmos. Chem. Phys.*, 20, 9591-  
767 9618, <https://doi.org/10.5194/acp-20-9591-2020>, 2020.
- 768 Sun, J., Zhang, K., Wan, H., Ma, P. L., Tang, Q., and Zhang, S.: Impact of nudging strategy on the climate  
769 representativeness and hindcast skill of constrained EAMv1 simulations, *Journal of Advances in Modeling Earth  
770 Systems*, 11, 3911-3933, <https://doi.org/10.1029/2019MS001831>, 2019.
- 771 Tang, Q., Klein, S. A., Xie, S., Lin, W., Golaz, J. C., Roesler, E. L., Taylor, M. A., Rasch, P. J., Bader, D. C., Berg,  
772 L. K., Caldwell, P., Giangrande, S. E., Neale, R. B., Qian, Y., Riihimaki, L. D., Zender, C. S., Zhang, Y., and  
773 Zheng, X.: Regionally refined test bed in E3SM atmosphere model version 1 (EAMv1) and applications for high-  
774 resolution modeling, *Geosci. Model Dev.*, 12, 2679-2706, <https://doi.org/10.5194/gmd-12-2679-2019>, 2019.
- 775 Van Marle, M. J., Kloster, S., Magi, B. I., Marlon, J. R., Daniau, A.-L., Field, R. D., Arneth, A., Forrest, M.,  
776 Hantson, S., and Kehrwald, N. M.: Historic global biomass burning emissions for CMIP6 (BB4CMIP) based on  
777 merging satellite observations with proxies and fire models (1750–2015), *Geoscientific Model Development*, 10,  
778 3329-3357, <https://doi.org/10.5194/gmd-10-3329-2017>, 2017.
- 779 Wan, H., Rasch, P. J., Taylor, M. A., and Jablonowski, C.: Short - term time step convergence in a climate model,  
780 *Journal of advances in modeling earth systems*, 7, 215-225, <https://doi.org/10.1002/2014MS000368>, 2015.
- 781 Wan, H., Zhang, S., Rasch, P. J., Larson, V. E., Zeng, X., and Yan, H.: Quantifying and attributing time step  
782 sensitivities in present-day climate simulations conducted with EAMv1, *Geoscientific Model Development*, 14,  
783 1921-1948, <https://doi.org/10.5194/gmd-14-1921-2021>, 2021.
- 784 Wang, H., Easter, R. C., Rasch, P. J., Wang, M., Liu, X., Ghan, S. J., Qian, Y., Yoon, J.-H., Ma, P.-L., and Vinoj,  
785 V.: Sensitivity of remote aerosol distributions to representation of cloud–aerosol interactions in a global climate  
786 model, *Geoscientific Model Development*, 6, 765-782, <https://doi.org/10.5194/gmd-6-765-2013>, 2013.
- 787 Wang, H., Easter, R. C., Zhang, R., Ma, P. L., Singh, B., Zhang, K., Ganguly, D., Rasch, P. J., Burrows, S. M., and  
788 Ghan, S. J.: Aerosols in the E3SM Version 1: New developments and their impacts on radiative forcing, *Journal of  
789 Advances in Modeling Earth Systems*, 12, e2019MS001851, <https://doi.org/10.1029/2019MS001851>, 2020.
- 790 Wang, J., Fan, J., Feng, Z., Zhang, K., Roesler, E., Hillman, B., Shpund, J., Lin, W., and Xie, S.: Impact of a new  
791 cloud microphysics parameterization on the simulations of mesoscale convective systems in E3SM, *Journal of  
792 Advances in Modeling Earth Systems*, 13, e2021MS002628, <https://doi.org/10.1029/2021MS002628>, 2021.
- 793 Wang, S., Maltrud, M., Elliott, S., Cameron-Smith, P., and Jonko, A.: Influence of dimethyl sulfide on the carbon  
794 cycle and biological production, *Biogeochemistry*, 138, 49-68, <https://doi.org/10.1007/s10533-018-0430-5>, 2018.
- 795 Wang, X., Zhang, R., and Yu, W.: The effects of PM<sub>2.5</sub> concentrations and relative humidity on atmospheric  
796 visibility in Beijing, *J. Geophys. Res.-Atmos.*, 124, 2235-2259, <https://doi.org/10.1029/2018JD029269>, 2019.

797 Wang, Y., Liu, X., Hoose, C., and Wang, B.: Different contact angle distributions for heterogeneous ice nucleation  
798 in the Community Atmospheric Model version 5, *Atmos. Chem. Phys.*, 14, 10411-10430,  
799 <https://doi.org/10.5194/acp-14-10411-2014>, 2014.

800 Xiao, Q., Zheng, Y., Geng, G., Chen, C., Huang, X., Che, H., Zhang, X., He, K., and Zhang, Q.: Separating  
801 emission and meteorological contributions to long-term PM<sub>2.5</sub> trends over eastern China during 2000–2018, *Atmos.*  
802 *Chem. Phys.*, 21, 9475-9496, <https://doi.org/10.5194/acp-21-9475-2021>, 2021.

803 Xie, S., Lin, W., Rasch, P. J., Ma, P. L., Neale, R., Larson, V. E., Qian, Y., Bogenschütz, P. A., Caldwell, P., and  
804 Cameron - Smith, P.: Understanding cloud and convective characteristics in version 1 of the E3SM atmosphere  
805 model, *Journal of Advances in Modeling Earth Systems*, 10, 2618-2644, <https://doi.org/10.1029/2018MS001350>,  
806 2018.

807 Zarzycki, C. M., Levy, M. N., Jablonowski, C., Overfelt, J. R., Taylor, M. A., and Ullrich, P. A.: Aquaplanet  
808 experiments using CAM's variable-resolution dynamical core, *J. Clim.*, 27, 5481-5503,  
809 <https://doi.org/10.1175/JCLI-D-14-00004.1>, 2014.

810 Zender, C. S., Bian, H., and Newman, D.: Mineral Dust Entrainment and Deposition (DEAD) model: Description  
811 and 1990s dust climatology, *J. Geophys. Res.-Atmos.*, 108, <https://doi.org/10.1029/2002JD002775>, 2003.

812 Zhang, G. J., and McFarlane, N. A.: Sensitivity of climate simulations to the parameterization of cumulus  
813 convection in the Canadian Climate Centre general circulation model, *Atmosphere-Ocean*, 33, 407-446,  
814 <https://doi.org/10.1080/07055900.1995.9649539>, 1995.

815 Zhang, K., Wan, H., Liu, X., Ghan, S. J., Kooperman, G. J., Ma, P.-L., Rasch, P. J., Neubauer, D., and Lohmann, U.:  
816 On the use of nudging for aerosol–climate model intercomparison studies, *Atmos. Chem. Phys.*, 14, 8631-8645,  
817 <https://doi.org/10.5194/acp-14-8631-2014>, 2014.

818 Zhang, K., Zhang, W., Wan, H., Rasch, P. J., Ghan, S. J., Easter, R. C., Shi, X., Wang, Y., Wang, H., and Ma, P.-L.:  
819 Effective radiative forcing of anthropogenic aerosols in E3SM version 1: historical changes, causality,  
820 decomposition, and parameterization sensitivities, *Atmos. Chem. Phys.*, 22, 9129-9160, <https://doi.org/10.5194/acp-22-9129-2022>, 2022a.

822 Zhang, S., Zhang, K., Wan, H., and Sun, J.: Further improvement and evaluation of nudging in the E3SM  
823 Atmosphere Model version 1 (EAMv1): simulations of the mean climate, weather events, and anthropogenic aerosol  
824 effects, *Geoscientific Model Development*, 15, 6787-6816, <https://doi.org/10.5194/gmd-15-6787-2022>, 2022b.

825 Zhao, C., Liu, X., Qian, Y., Yoon, J., Hou, Z., Lin, G., McFarlane, S., Wang, H., Yang, B., and Ma, P.-L.: A  
826 sensitivity study of radiative fluxes at the top of atmosphere to cloud-microphysics and aerosol parameters in the  
827 community atmosphere model CAM5, *Atmos. Chem. Phys.*, 13, 10969-10987, <https://doi.org/10.5194/acp-13-10969-2013>, 2013.

829